J. Fluid Mech. (2007), *vol.* 576, *pp.* 191–233.
doi:10.1017/S0022112006004393 Printed in the United Kingdom

Cavitation microstreaming patterns in single and multiple bubble systems

PAUL THO[1], RICHARD MANASSEH[2] AND ANDREW OOI[1]

[1]Department of Mechanical and Manufacturing Engineering, The University of Melbourne, Parkville, Victoria, 3010, Australia

[2]CSIRO Manufacturing and Infrastructure Technology, PO Box 56, Highett, Victoria, 3190, Australia

richard.manasseh@csiro.au; a.ooi@unimelb.edu.au

(Received 27 March 2006 and in revised form 25 September 2006)

Cavitation microstreaming is a well-known phenomenon; however, few flow visualizations or measurements of the velocity fields have been conducted. In this paper micro-PIV (particle image velocimetry) measurements and streak photography were used to study the flow field around a single and two oscillating bubbles resting on a solid boundary. The mode of oscillation of the bubble was also measured in terms of the variation in the radius of the bubble and the movement of the bubble's centroid so that the streaming flow field could be accurately related to the bubble's oscillatory motion. The mode of oscillation was found to vary primarily with the applied acoustic frequency. Several modes of oscillation were investigated, including translating modes where the bubble's centroid moves along either a single axis, an elliptical orbit or a circular orbit. The flow field resulting from these oscillation modes contains closed streamlines representing vortical regions in the vicinity of the bubble. The translating modes were observed to occur in sequential order with the acoustic excitation frequency, changing from a translation along a single axis, to an elliptical orbit and finally to a circular orbit, or vice versa. Following this sequence, there is a corresponding transformation of the streaming pattern from a symmetrical flow structure containing four vortices to a circular vortex centred on the bubble. Despite some inconsistencies, there is general agreement between these streaming patterns and those found in existing theoretical models. Volume and shape mode oscillations of single bubbles as well as several different cases of multiple bubbles simultaneously oscillating with the same frequency and phase were also investigated and show a rich variety of streaming patterns.

1. Introduction

1.1. *Background*

A body oscillating in a viscous fluid generates fluctuations in velocity and pressure in the fluid surrounding it. The temporal average of these fluctuations is often non-zero and results in a steady streaming flow. When the body is a gas bubble, the small-scale streaming flow is referred to as 'cavitation microstreaming'. Similar streaming flows are also observed around solid objects (e.g. a cylinder or sphere) undergoing small-amplitude oscillations. Steady streaming flows are reviewed extensively by Riley (1965, 2001) and Nyborg (1965, 1998), who also discuss 'acoustic streaming', a phenomenon

related to the attenuation of acoustic energy as a sound wave passes through a fluid. Although cavitation microstreaming may also be instigated by an acoustic source, the mechanism driving the flow field is different. This study is concerned only with bubble induced microstreaming.

Cavitation microstreaming results from vorticity generated within the oscillatory boundary layer surrounding the bubble and is a consequence of second-order nonlinear terms in the vorticity transport equation. At leading order, the flow outside the boundary layer is irrotational. However, within the oscillatory boundary layer, also referred to as the Stokes layer or shear wave layer, Reynolds stresses drive a steady streaming which extends to the edge of the boundary layer. This apparent slip velocity drives the outer streaming well beyond the Stokes layer (Lee & Wang 1990).

The streaming flow pattern that is observed depends on the mode of oscillation of the bubble. Bubbles may undergo several different types of oscillatory motions. These include translating oscillations where the bubble moves periodically along one or more different axes. The simplest case for a translating motion is a harmonic translation along a single axis, while others might include orbiting motions. Another mode of oscillation is that of a bubble undergoing volume oscillations, where the bubble expands and contracts radially while maintaining its spherical shape. This is also known as the 'breathing' mode. This behaviour is a consequence of the compressibility of the gas and is forced by the fluctuating acoustic pressure field. This oscillatory mode is most pronounced when the bubble is excited near its natural frequency, which for a spherical bubble can be estimated using Minnaert's equation (Minnaert 1933)

$$f_M = \frac{1}{2\pi R_0}\sqrt{\frac{3\gamma p_0}{\rho}}, \tag{1.1}$$

where f_M is the linear resonance frequency, R_0 is the bubble's equilibrium radius, γ is the ratio of specific heats of gas, p_0 is the hydrostatic liquid pressure and ρ is the density of the liquid. Finally, bubbles may also be excited into higher-order modes of oscillation where the surface of the bubble deforms into polygonal shapes.

1.2. *Experimental studies*

Although cavitation microstreaming is a phenomenon that has been observed and studied since the 1950s, there are limited flow-visualization data and experimental studies of how the mode of oscillation affects the type of flow pattern. Kolb & Nyborg (1956) were the first to study cavitation microstreaming. They observed that the streaming is orderly at low driving amplitudes, and is most pronounced when a bubble is resting on a solid boundary and in volume oscillation. Elder (1959) followed on from their work and studied the effects that the amplitude of oscillation and fluid viscosity have on the streaming patterns of a bubble resting on a solid boundary. The modes of oscillation that were studied included volume oscillations and surface wave modes. He classified the patterns into four streaming regimes and recorded these observations as a series of sketches. The sketches depict streaming flows which contain one or more vortices surrounding the bubble. Although the sketches provide the salient features of the flow field, they are qualitative and do not provide information on the fine details of the flow structures.

The majority of the studies into cavitation microstreaming thus far have focused on the applications it has to biological systems and in engineering applications, rather

than fundamental studies of the physics of the fluid flow. Recently, interest in the application of this field to microfluidics has grown. Liu *et al.* (2002) demonstrated the effectiveness of cavitation microstreaming as a mechanism for mixing fluids at the microscale. Their experimental system, similar to the one used in the present experiments, consists of a microchamber with a piezoelectric disk attached to one of its walls which provides the acoustic excitation of the bubbles inside the chamber. Vigorous eddying motions inside the chamber were observed whenever the bubbles were excited. The authors used dyes to visualize the flow field and describe the flow pattern as 'tornado' like with streaming velocities of approximately $5\,\mathrm{mm\,s^{-1}}$. Although the dyes clearly show a streaming pattern in the vicinity of the bubble, the dyes do not adequately show its fine vortex structures and the flow descriptions are limited. Furthermore, there is little information regarding the mode of oscillation of the bubble.

Marmottant & Hilgenfeldt (2004) studied the flow field around an oscillating bubble, suggesting it could be used to transport particles in a microfluidic device. They showed that if a stationary particle is placed in the vicinity of a bubble undergoing cavitation microstreaming, then this particle will also develop a streaming flow around it. A series of these bubble–particle pairs can be positioned in such a way that fluid elements are transported systematically. The authors studied the flow behaviour by tracing the motion of a lipid vesicle as it moves between the bubble and a solid particle. A numerical calculation of the streamlines induced by the bubble–particle pair was shown to be in qualitative agreement with their experimental observations.

In earlier related work, Marmottant & Hilgenfeldt (2003) showed that by introducing lipid vesicles into a solution they were able to track the streamlines around an oscillating bubble. These experiments were particularly interesting because a lipid vesicle could be a model for a biological cell. The streaming flows observed consist of a vortex ring around the bubble. In one experiment, they show that a vesicle caught in the core of a vortex could be ruptured owing to the shearing forces in the vicinity of the core. The lipid vesicle used to track the fluid flow was of the same order in size as the bubble. Tracing streaming flows requires seed particles that are small enough to accurately follow the fluid streamlines, otherwise there may be a considerable lag in the actual fluid velocity. It appears that the size of the lipid vesicles contributed to the apparent difference between the fluid motion traced out by the vesicle and that of an analytical solution for the flow field. Also the use of individual lipid vesicles limits the flow visualization to a few streamlines. In the present experiments, very small flow tracer particles are used to image the streamlines and measure the entire velocity field.

There are numerous biological effects related to cavitation microstreaming. Rooney (1989) observed that the shearing stresses due to cavitation microstreaming caused haemolysis of erythrocytes, supporting the observations made by Marmottant & Hilgenfeldt (2003). Pritchard, Hughes & Peacocke (1966) observed DNA degradation as a result of shear stresses at sonic amplitudes below the threshold for cavitation. The shearing action of microstreaming flows has also been proposed as a mechanism for sonoporation which can be used for gene and drug transfection using contrast agents (Gormley & Wu 1998; Wu, Ross & Chiu 2002). Also numerical calculations of the shear forces induced by cavitation microstreaming have been found to be large enough to generate reparable sonoporation (Lewin & Bjørnø 1982; Wu 2002). Besides these biological effects, the microstreaming flows also have implications in the transport of species in sonochemical (Rosenthal, Sostaric & Riesz 2004), sonoluminescent (Verraes *et al.* 2000) and in sonic cleaning processes (Shoh 1975). Finally, it has also been shown that microstreaming flows influence the mass diffusion of gas into or out of

the bubble (Gould 1974; Davidson 1971) owing to the streaming flow around it and rectified diffusion.

1.3. *Theoretical studies*

Although there are few fundamental experimental studies of microstreaming flows, there are several well-developed theoretical studies. Many of these are extensions to earlier work involving solid bodies undergoing small-amplitude oscillations. The cylinder and sphere have received particular attention and show streaming patterns that are qualitatively similar to what is observed around bubbles owing to their geometric similarity (Holtsmark *et al.* 1954; Davidson & Riley 1972; Riley 1975; Amin 1988; Lee & Wang 1990). Several important parameters are often cited in the study of oscillating bodies. If a body is performing a harmonic oscillation in an unbounded fluid, which is otherwise still, then the motion of the body may be described as $U\cos\omega t$, where U is a velocity scale of the body's oscillation and ω is the angular frequency of oscillation. Then if d is a characteristic length scale of the body, and ν is the kinematic viscosity of the fluid, the important dimensionless streaming parameters are defined by Riley (1967) as

(i) $\epsilon = U/\omega d$, where ϵ may be interpreted as the ratio of the amplitude of oscillation to a body length scale. It is the inverse of the Strouhal number. In all cases studied, it is assumed the oscillations are of small amplitude, i.e. $\epsilon \ll 1$.

(ii) $M^2 = \omega d^2/\nu$, where M may be interpreted as the ratio of the body length scale to a viscous length scale $(\nu/\omega)^{1/2}$.

(iii) $R_s = U^2/\omega\nu = \epsilon^2 M^2$, where R_s is the streaming Reynolds number which characterizes the flow field outside the Stokes layer.

The theory for the streaming around oscillating bubbles has been developed for bubbles undergoing harmonic translating and volume oscillation modes. The important difference between oscillating solid bodies and bubbles is the boundary conditions. Solid objects have a 'no-slip' boundary condition on their surfaces, whereas for bubbles, there is no radial velocity and zero shear stress at the air–water interface. Davidson & Riley (1971) investigated the streaming around a spherical bubble undergoing a harmonic translating oscillation along a single axis in an unbounded fluid, although they frame the problem as analogous to a sound wave incident on a stationary bubble. The authors studied two different cases: $M \ll 1$, where the vorticity is diffused over a relatively large distance; and $M \gg 1$, where it is confined within the thin Stokes layer. They showed that these different conditions produce a reversal in the flow direction and that the streaming velocities are $O(\epsilon M^2 U)$ for $M \ll 1$ and $O(\epsilon U/M)$ for $M \gg 1$.

Longuet-Higgins (1998) extended the work of Davidson & Riley by studying the streaming behaviour of a bubble simultaneously undergoing translating oscillations along a single axis and volume oscillations seen as radial pulsations of the bubble wall. Without the radial pulsations present, the streaming flow pattern was described as a 'quadrupole' owing to the hyperbolic streamline patterns around the bubble. With the addition of radial pulsations to the bubble, the streaming pattern was described as a 'dipole'. Wu & Du (1997) also studied the translating and volume oscillating modes and showed similar streamline patterns around the bubbles. Their study of the volume only oscillation mode shows that the directionality of the streaming flow results from the direction of the propagating pressure wave. To our knowledge, there are no theoretical studies of the streaming flows around bubbles resting on a solid boundary, where they often become hemispherical in shape. Furthermore, there have not been any experimental or theoretical studies investigating the streaming induced

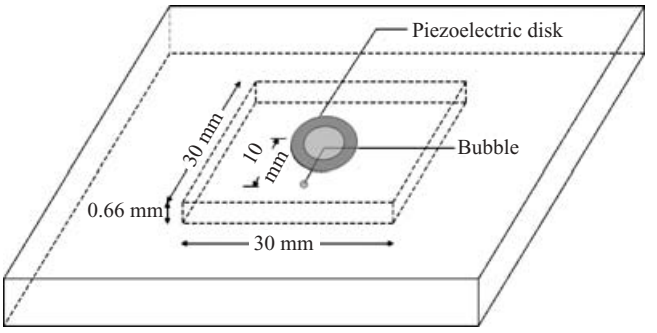

FIGURE 1. Schematic of the microchamber.

by bubbles undergoing shape mode oscillations, bubbles moving in elliptical orbits or from a pair of oscillating bubbles.

The limited experimental study of cavitation microstreaming may perhaps relate to the difficulty in measuring the flow fields with sufficient spatial resolution. With the advent of micro-PIV (micro-particle image velocimetry) it is now possible to do so. The present study seeks to further earlier experimental studies in cavitation microstreaming of bubbles attached to a wall by providing photographic flow visualization of the flow fields, measurements of the velocity fields and correlation of this data to the mode of oscillation of the bubble, including several modes that have not been observed before. The modes of oscillation that are studied include several different translating, volume and shape mode oscillations. The mode of oscillation is characterized by measuring the translating motions of the bubble's centroid as well as variation in its radius. Ultimately, the data in this study provide a qualitative and quantitative link between the mode of oscillation of the bubble and the resulting streaming flow pattern. The scope of this study is limited to fluids of low viscosity in the regime of $\epsilon \ll 1$, $M^2 \gg 1$ and $R_s = O(1)$. The work will also investigate the microstreaming flows around several cases of pairs of bubbles undergoing various modes of oscillation. The experimental parameters that are adjusted during the course of the experiment are the applied acoustic pressure amplitude and frequency. The size of the bubbles remains roughly constant ($\sim$250 μm in radius) throughout the different sets of experiments.

The paper is organized as follows. In § 2, the details of the experimental system and methods used to study the streaming flows and oscillatory motion of the bubble are described. Section 3 provides some background experimental measurements to give context to the main experiments. Section 4 provides the main experimental results of the microstreaming flows around single bubbles, followed by § 5 which details the flow around multiple bubbles under several different modes of oscillation. Section 6 discusses observations of the enhanced growth in the size of a bubble owing to microstreaming and finally, § 7 summarizes the main findings.

2. Experimental apparatus and method

2.1. *Microchamber*

Cavitation microstreaming is induced around bubbles placed within an enclosed chamber which will be referred to as a 'microchamber' because of its sub-millimetre depth (figure 1). The system presents a different environment to the free-field conditions that theoretical analysis has been developed for (Davidson & Riley 1971;

Longuet-Higgins 1998; Wu & Du 1997). The important characteristics of the system are:

(*a*) The streaming takes place around bubbles that are attached to a wall and as a consequence are distorted in shape and are approximately hemispherical.

(*b*) For the majority of experiments, the bubbles are attached to the upper wall of the microchamber.

(*c*) The streaming is confined between two plane walls in close proximity.

These features share similarities with those of the experimental work of others. Marmottant & Hilgenfeldt (2003) and Elder (1959) studied the streaming around hemispherical bubbles attached to a single wall. However, their systems were much larger than that used here where the fluid and bubble motion are in a confined environment. Liu *et al.* (2002) studied the streaming that is confined between two plane walls; however, the bubbles in their experiment were cylindrical in shape as a consequence of being sandwiched between two walls. In all earlier experiments, the bubbles are attached to the bottom wall as 'pendent bubbles' and are held in position by surface tension forces (Thiessen & Man 1998). In the present experiments, the majority of bubbles are held on the upper surface as 'captive bubbles' by both surface tension and natural buoyancy (Thiessen & Man 1998).

The microchamber is a thin square cross-sectional chamber of dimensions $30 \times 30 \times 0.66\,\mathrm{mm}^3$ enclosing a volume of roughly 594 µl. The chamber is made of optically transparent polycarbonate with a detachable Perspex cover. The acoustic source which excites the bubbles is a thin 12 mm diameter lead zirconate titanate (PZT) piezoelectric disk (APC International) which is centrally attached to the outer polycarbonate wall. The disk has a nominal resonance frequency of 9.5 ± 1.0 kHz and was selected because its frequency of peak response closely matched the bubble's natural frequency as estimated by (1.1).

The microchamber is filled with a solution containing micrometre sized flow tracer particles. An air bubble is then attached to the polycarbonate wall using an injection syringe (Hamilton Gastight®, 10 µl) and needle (0.11 mm internal diameter). The bubble is placed 10 mm from the centre of the piezoelectric disk where there is ease of optical and illumination access. The chamber is then placed under a microscope for viewing with the bubbles in either a captive or pendent position. Captive bubbles rest on the upper wall of the microchamber and remain attached as a result of buoyancy as well as surface tension. Pendent bubbles are attached to the bottom surface and are held in position by surface tension forces. The majority of bubbles in the present streaming experiments are captive bubbles.

2.2. *Acoustic excitation system*

The piezoelectric disk attached to the microchamber is connected via electrical leads to a signal generator (Wavetek Model 145) which delivers a sinusoidal electrical waveform causing the piezoelectric ceramic to vibrate at the same frequency. The waveform frequency is varied from 0 to 20 kHz in increments of 0.25 ± 0.005 kHz, and the voltage amplitude between 15 and 30 V_{pp} in increments of $5 \pm 0.05\,V_{pp}$. These input parameters are determined through an oscilloscope (Tektronix TDS 210) connected to the signal generator.

The sound pressure levels emitted by the piezoelectric disk vary nonlinearly with its excitation frequency. To determine the actual pressure delivered through the walls of the chamber, the pressure amplitude P was measured as a function of the input signal frequency f and voltage amplitude. These were recorded using a hydrophone positioned inside a replica chamber with the same cross-sectional dimensions, but with a depth of 2 cm. This depth ensured enough wetted area for the hydrophone to

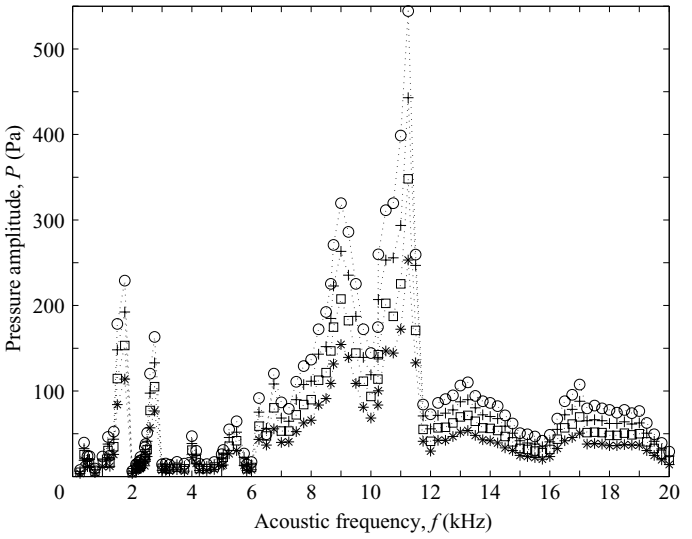

FIGURE 2. The acoustic pressure amplitude P delivered by the piezoelectric disk versus excitation frequency f for voltage amplitudes of 30 V_{pp} (○), 25 V_{pp} (+), 20 V_{pp} (□) and 15 V_{pp} (✳).

take measurements. The chamber was filled with 1 cm of water and a hydrophone (Brüel & Kjær Type 8103, with a 9.5 mm diameter) placed directly above the position in which a bubble normally rests. The sinusoidal electrical signal received by the hydrophone is passed through a charge amplifier (Brüel & Kjær Type 2635) which is relayed to an oscilloscope for measurement. This signal was then averaged out over 128 waveforms to remove noise and the peak amplitude of this waveform measured and converted to a pressure scale by a conversion factor of 31.65 Pa V^{-1} determined from the hydrophone and charge amplifier settings. The error of these measurements is estimated to be approximately ± 1.6 Pa.

The results are plotted in figure 2 and show resonances in the system at the nominal resonance frequency (~9.5 kHz), but also at several other frequencies with pressure amplitudes up to 550 Pa.

2.3. *Flow tracers*

The tracer particles used for flow visualization are 2 μm diameter polystyrene fluorescent microspheres (Duke Scientific). The microspheres are coated in a red dye that is excited at a wavelength of light of 542 nm (green), and which fluoresce at a wavelength of 612 nm (red). The particles are packaged in an unspecified diluent to prevent the particles from clumping. This is then diluted with analytical grade de-ionized water to give a final concentration of 6.52×10^7 particles ml^{-1} or 0.027 % by volume fraction.

The tracer particle images are resolved over roughly 4–5 pixels according to the formulation provided by Adrian & Yao (1985). The particle image must be large enough to be resolved so that its displacement can be calculated in micro-PIV analysis. Wereley & Meinhart (2003) suggest that particle images should be resolved over at least 3–4 pixels in micro-PIV experiments to provide accurate particle displacement measurements.

While the particles must be large enough to be adequately imaged, they must also follow the moving fluid with fidelity. This is dependent on several factors. First, the

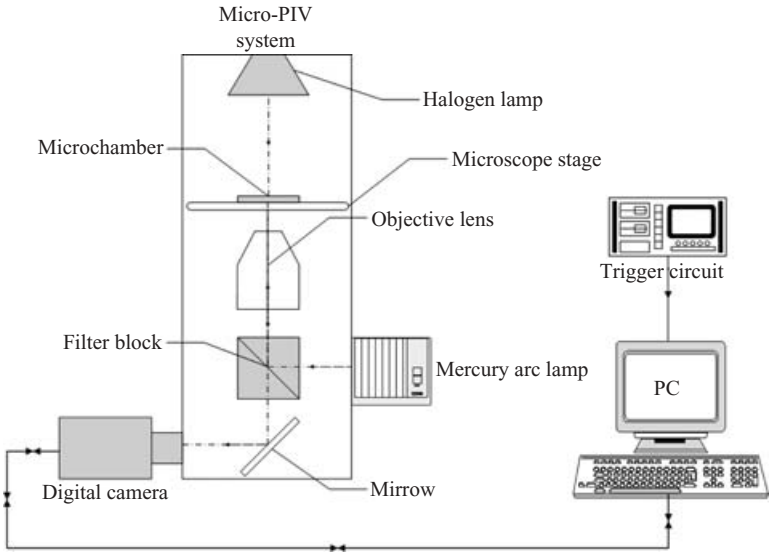

FIGURE 3. Schematic of the micro-PIV system.

polystyrene particles are density matched ($1.05\,\mathrm{g\,cm^{-3}}$) with surrounding fluid which minimizes gravity and buoyancy-induced velocities which cannot be resolved depth wise in two-dimensional micro-PIV measurements. The response time of the particles, as a measure of its ability to move through accelerating regions of fluid, was found to be roughly 2.3×10^{-7} s (Wereley & Meinhart 2003) which is deemed to be sufficiently small enough for these experiments. Also, a consideration of the velocity lag of a flow tracer relative to the surrounding fluid shows this is less than 1 % of the streaming velocities encountered in these experiments (Adrian 1991). Likewise, a consideration of the Brownian motion of the particles suggests an error less than 0.35 % of the velocities measured in these experiments (Devasenathipathy *et al.* 2003).

2.4. *Experimental imaging*

2.4.1. *Micro-particle image velocimetry system*

The micro-PIV system used in these experiments consists of an inverted epi-fluorescent microscope (Nikon TE2000-E), a mercury arc lamp for epi-fluorescent imaging, a halogen lamp for brightfield imaging, a digital CCD camera (PCO Sensicam QE®) and an external trigger circuit (figure 3). The micro-PIV system is used to take streak photographs depicting the streamlines of the flow field, micro-PIV image pairs used in cross-correlation analysis to determine the instantaneous velocity fields and also images depicting the oscillatory motion of the bubble.

The two illumination sources are used in different imaging methods. The mercury arc lamp is used in streak photography and micro-PIV imaging. It is used to induce fluorescence of the microsphere particles. A set of filters (Chroma Technology) housed in a filter block in the microscope ensures the appropriate narrowband wavelength of light (532 nm) excites the particles, and that the emitted fluorescent light (612 nm) is imaged while the majority of background light is filtered out. This ensures good contrast between the particle images and the background. It should be noted that pulsed laser beams are the preferred illumination source for micro-PIV experiments because this allows shorter exposure times for imaging. However, such a system had not yet been set up at the time of the experiments. The halogen lamp is used for

brightfield microscopy where light is transmitted through the microchamber. This mode of microscopy is used to image the bubbles as they are undergoing oscillatory motion.

The objective lens used in these experiments is a Nikon CFI 60 Plan Fluor 4× objective lens with a numerical aperture of 0.13. In micro-PIV, the entire volume of fluid is illuminated and a thin imaging plane is reliant on the small depth of field of the objective lens. Therefore, out-of-focus particles will have an impact on the degree of accuracy of micro-PIV particle displacement analysis. The depth of correlation δz_m is a measure of this effect for volume illuminated micro-PIV. Using the formulation provided by Meinhart, Wereley & Gray (2000), the depth of correlation in these experiments is $\delta z_m = 144\,\mu\text{m}$. The depth of correlation is relatively large compared to the size of the bubble, therefore the velocity data contain a significant depthwise-averaged velocity component.

The images are recorded on a 12 bit, 1248 × 1024 pixel resolution digital CCD camera. The image scale was determined using an objective micrometer in which the field of view for a 1248 × 1024 resolution image equates roughly to $2.204 \times 1.661\,\text{mm}^2$. Camera exposure time, frame rate and time delay between images are set through either the camera control software or externally from a TTL signal from an trigger circuit built in house.

2.4.2. *Streak photography*

Streak photographs directly image the streamlines of the flow field. This involves initiating epi-fluorescence in the microspheres and then filtering out the majority of background light so that the CCD can be exposed for longer periods, leaving a 'streak' of light left behind by the microspheres. The CCD camera is set to record continually a series of streak photos with an exposure time of 1 s and at a frame rate of 1 frame per second (f.p.s.). The images are taken along three different focal planes which cover three different regions of the bubble, and are located at different distances from the wall that the bubble is attached to: near the base of the bubble ($z_1 = 75\,\mu\text{m}$ plane), near the middle–upper region ($z_2 = 300\,\mu\text{m}$ plane) and away from the bubble ($z_3 = 525\,\mu\text{m}$ plane). The positions of these focal planes were determined from a remote-control reading of the relative change in height of the objective lens, using the wall that the bubble is attached to as the reference plane.

2.4.3. *Micro-PIV measurements*

Micro-PIV image pairs were recorded using epi-fluorescent microscopy with an exposure time of 10 ms and a time interval of 35 ms between the pair of images. The camera's image exposure and triggering were controlled with an external trigger control circuit. Ten image pairs were recorded along each focal plane (z_1, z_2 and z_3) for ensemble averaging.

Analysis of the micro-PIV images was carried out using a standard cross-correlation algorithm implemented in a commercial PIV software package (VISIFLOW®, AEA Technology). The interrogation regions are 128 × 128 pixels with an overlap of 75 % to maximize the available data. This results in a vector spacing of 32 pixels or roughly 52 μm in the x- and y-directions. The correlation peak is detected via a simple maximum-value search to locate the coordinate position of the most dominant correlation peak. The accuracy of peak detection is improved to subpixel accuracy by fitting a two-dimensional Gaussian function using the surrounding 25 (5 × 5 grid points) correlation coefficients. This analysis is carried out for all 10 image pairs along each focal plane, and the velocity vectors are then ensemble averaged.

2.4.4. *Bubble dynamics measurements*

Brightfield microscopy was used to image the oscillatory motion of the bubble. It was necessary to choose the smallest possible exposure time so that a bubble could be 'frozen' in its oscillation otherwise any oscillatory motion would blur out. A 10 μs exposure time was used to record these images, and was the smallest exposure time possible without the image being too grainy. The frequency of oscillation for the majority of the bubbles is under 5 kHz, therefore the image will record at most 5 % of the bubble's oscillation cycle.

Two aspects of the bubble's oscillatory motion are of interest: the translating path the bubble moves through; and the variation in the bubble's radius over an oscillation cycle. To image the translating motion of the bubble, 50 images were recorded continuously at a rate of 10.11 f.p.s. This frame rate is clearly too low to be able to resolve the motion of a bubble temporally over an oscillation cycle (typically milliseconds). However, this was not its intention, rather its purpose was to obtain a large number of images so that the centroid of the bubble could be tracked over many images and provide a spatial x–y map of points that the centroid moves through, e.g. an elliptical or linear path.

To image the variation in the bubble's radius over an oscillation cycle, the images were phase locked with the oscillation cycle. The signal from the signal generator initiates a pulse signal in a trigger circuit with the same frequency as that of the sinusoidal waveform. The pulse signal triggers the camera, and its phase is adjusted in intervals of $\pi/4$ over 2π. Thus, these images can be used to reconstruct an entire cycle sampled at each phase-locked position. Four images were taken at each phase-locked position and then averaged.

To determine the bubble's centroid and radius from the grey-scale image, the shape of the bubble was extracted from the rest of the image using a Canny edge detection algorithm (Canny 1986). This converts the image to a binary image containing the pixels on the bubble's edge boundary from which the image centroid is calculated. The results are non-dimensionalized as the spatial coordinates η_x and η_y using

$$\eta_x = \frac{x_i - x_{eq}}{R_0}, \tag{2.1a}$$

$$\eta_y = \frac{y_i - y_{eq}}{R_0}, \tag{2.1b}$$

where x_i and y_i are the instantaneous centroid coordinates, x_{eq} and y_{eq} are the equilibrium centroid coordinates and R_0 is the bubble's equilibrium radius. The coordinates measure the amplitude of oscillation scaled against the radius of the bubble and are equivalent to the non-dimensionalized parameter ϵ described in § 1, and also allow us to determine M^2 and R_s.

The bubble's radius is measured from a rectangular bounding box fitted around the edge of a bubble. The bounding box provides a simple estimate of the bubble diameter. It assumes the bubble's edge is roughly circular with little variation in the length and width of the bounding box. This is justified in this experiment as the difference in these measurements is less than 1.5 % of the bubble diameter. The length and width of the bounding box are averaged as a final estimate of the bubble diameter. The radius is expressed as the non-dimensional parameter η_r and is defined as

$$\eta_r = \frac{R_i - R_0}{R_0}, \tag{2.2}$$

where R_i is the instantaneous radius and R_0 is the equilibrium radius. The

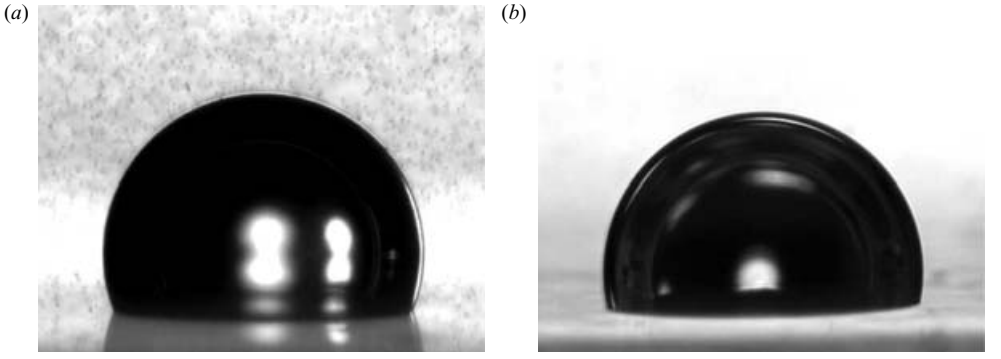

FIGURE 4. Images of the profile of a bubble in the (*a*) microsphere solution and in (*b*) purified water.

edge-detection, centroid and radius-finding algorithms described above were implemented through MATLAB®. The details of the experimental system and the calculations of the flow tracing and imaging characteristics of the system are presented in detail by Tho (2005).

3. Preliminary experimental measurements

3.1. *Bubble profile*

A bubble attached to a wall will deform from its usual spherical shape. The extent of deformation depends on the surface tension of the material the bubble is attached to and that of the surrounding liquid. The shape of the bubble is important when considering the reliability of any comparisons made between the experimental results and the theoretical models which assume a spherical bubble. To image the side profile of bubbles, images were recorded of a bubble resting on a polycarbonate surface perpendicular to the focal plane since it is not possible to view the side profile of the bubble ordinarily. This bubble configuration is neither a captive nor pendent bubble. However, because of the small size of the bubble, the surface tension is expected to dominate over buoyancy and gravity forces which would slightly alter the shape of the bubbles between these two positions. Hence, small bubbles should maintain their shape from one configuration to another and using an 'in between' configuration provides a reasonable estimate of the actual shape of bubbles in the experiment. Several images were taken of bubbles with diameters between 462 and 584 μm in the microsphere solution and the shape and contact angle of the bubbles were found to be consistent. Figure 4(*a*) shows the shape of a 526 μm diameter bubble.

Figure 4(*b*) is an image of a 521 μm diameter bubble in filtered analytical grade water and represents the shape of a 'clean' bubble with no impurities or surface skin at the air–water interface. Several images were taken of these bubbles with diameters between 467 and 581 μm, showing that there was little variation in their shapes. Comparing figures 4(*a*) and 4(*b*) there is a noticeable difference in their shapes. The bubbles in pure water appear flatter and more hemispherical in shape than bubbles in the microsphere solution. This implies that there is a difference in the surface tension of the bubbles which may be due either to a localized effect of a surface skin on the bubble made of the microsphere's diluent or to a difference in the surface tension of the bulk solutions. The importance of this relates to the boundary conditions of the bubbles. The fluid motion over bubbles which have a surface skin may be inhibited in

a manner similar to a 'no-slip' condition for solid bodies. This is in contrast to 'clean' bubbles which are modelled with a 'free-slip' boundary. Elder (1959) showed that when a surface skin formed around a bubble, the fluid moved away from the bubble along its axis of oscillation. When the surface skin broke up, the direction reversed.

3.2. *Factors that influence cavitation microstreaming*

Initial experiments showed that cavitation microstreaming was readily observed around bubbles in the microchamber whenever the piezoelectric disk was activated. It is certain that the streaming motions around the bubble were induced by vibrations in the bubble and were not caused by acoustic streaming from the attenuation of sound in water (Riley 2001) since streaming could not be detected without bubbles present. Furthermore, the movement of fluid is confined to the region around the bubble with no appreciable motion in fluid far removed from the oscillating bubble. There are several parameters than can be readily adjusted that affect the microstreaming. These include the frequency and voltage amplitude of the excitation signal that drives the piezoelectric disk and the size of the bubble.

3.2.1. *Effects of the acoustic frequency*

A variation in the acoustic frequency results in changes in the streaming pattern. The majority of these streaming patterns exhibit some regularity or symmetry. As the frequency is varied, the streaming pattern typically varies, smoothly changing between symmetric and asymmetric patterns. However, occasionally a sudden change in streaming pattern occurs. There would be either a reversal in flow direction or the sudden onset of a completely new mode of streaming, such as when a bubble suddenly exhibits a shape or volume oscillation. Figure 5 shows a series of streak photographs of the streaming flow around a 272 μm radius captive bubble at different acoustic excitation frequencies. The wide variety of streaming motions observed indicates the degree of variety in the modes of oscillation of bubbbles that are induced in this system.

The variations in streaming pattern must be associated with different modes of oscillation of the bubble since streaming is not observed without any bubbles present. Symmetrical streaming patterns would presumably be caused by symmetrical modes of oscillation, and asymmetric streaming patterns as a result of asymmetric modes of oscillation. The fact that the streaming patterns change with different frequencies implies that altering the piezoelectric frequency must also alter the form of the sound waves set up in the microchamber. Depending on the form of the sound wave, the resulting acoustic radiation pressure will act on the bubble in different ways to induce a variety of translating motions of the bubble.

3.2.2. *Effects of bubble size*

For a given acoustic excitation frequency, a variation in the bubble size will also affect the streaming flow pattern. Presumably this is related to differences in the way the acoustic radiation pressure acts on different sized bubbles. Figure 6 shows the streaming patterns around different sized captive bubbles each excited with a 4 kHz acoustic frequency. The streaming patterns observed within the range of bubble sizes tested do not vary as dramatically as those found when the acoustic frequency was varied. This is most probably because, unlike varying the acoustic frequency, the form of the acoustic radiation force itself is not being altered, rather the size of the bubble simply changes how it influences the bubble. Since the bubbles are located at the same position in the microchamber, it is unsurprising that the relatively small variations in the size of the bubble do not induce dramatic variations in the streaming flow patterns.

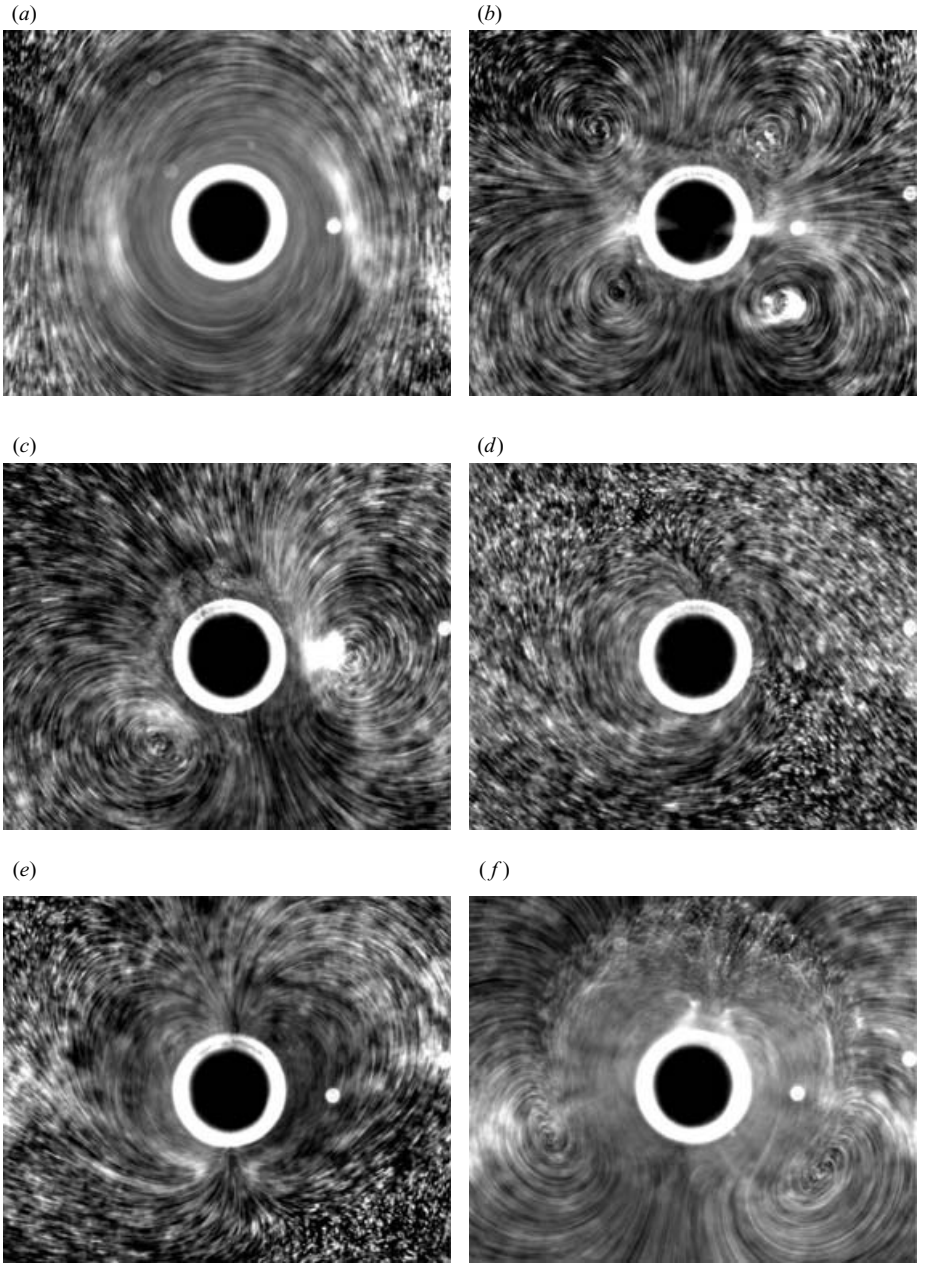

FIGURE 5. Streaming patterns around a 272 μm radius bubble excited at acoustic frequencies of (*a*) 1 kHz, (*b*) 3 kHz, (*c*) 4 kHz, (*d*) 7 kHz, (*e*) 9 kHz and (*f*) 11 kHz.

4. Microstreaming around single bubbles

The study of cavitation microstreaming around a single bubble covers seven different modes of oscillation of the bubble. Cases 1–3 (see table 1) are purely translating oscillation modes where the centroid of the bubble moves along a single axis, an elliptical orbit and a circular orbit. Cases 2(*a*) and 2(*b*) represent elliptical orbits of different eccentricity. Case 4 is a bubble primarily undergoing a volume

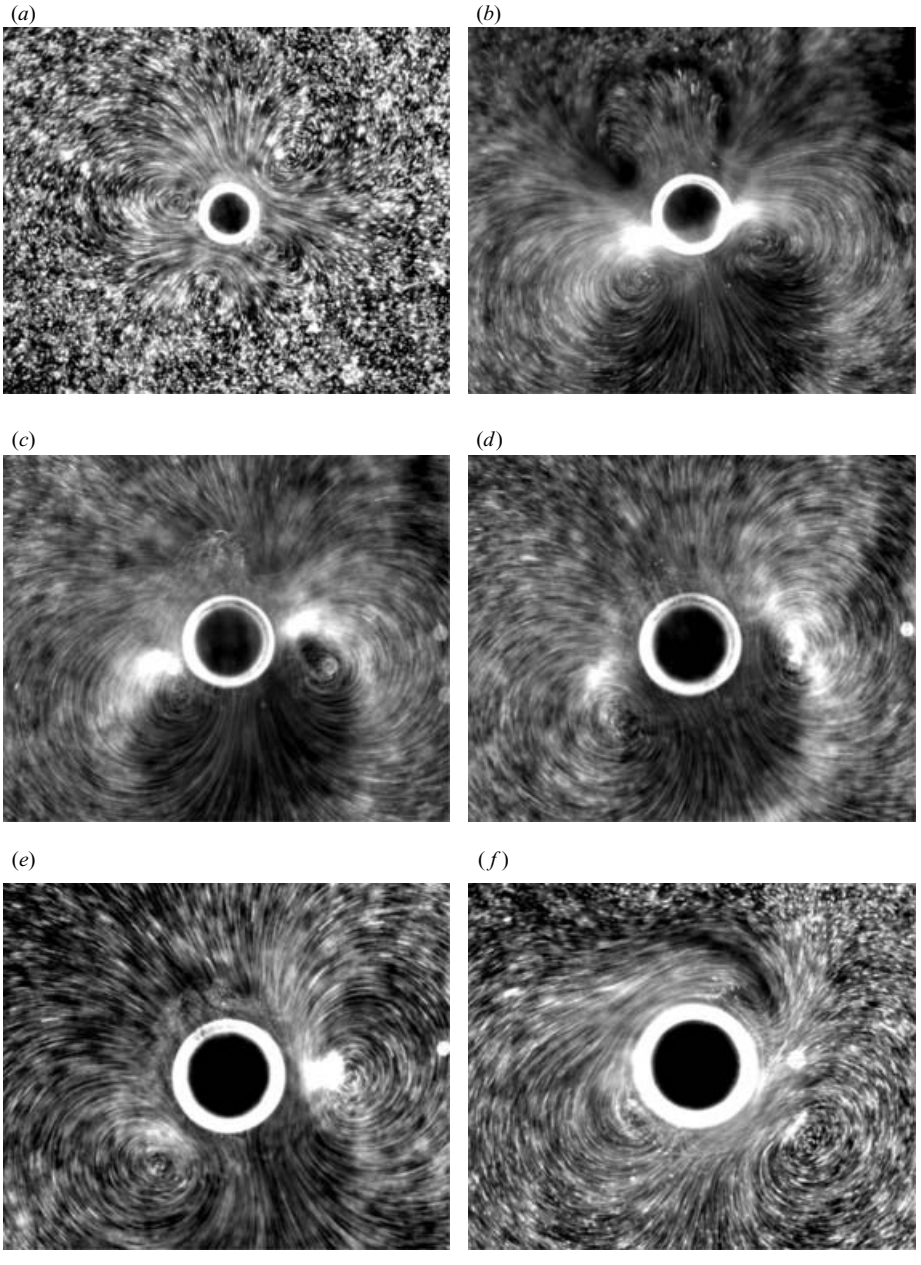

FIGURE 6. Streaming patterns induced at a 4 kHz acoustic frequency around bubbles with a radius of (*a*) 136 μm, (*b*) 181 μm, (*c*) 217 μm, (*d*) 241 μm, (*e*) 272 μm and (*f*) 294 μm.

oscillation, while Case 5 includes the superpose of a translating oscillation over this. Case 6 studies a bubble whose centroid translates along an axis perpendicular to the wall it is attached to and Case 7 studies bubbles undergoing several different shape mode oscillations. Each of these modes of oscillation was studied under different experimental conditions, in particular under different acoustic excitation frequencies. The accuracy of the applied acoustic frequency reading is roughly ± 0.05 kHz. A summary of the experimental conditions is shown in table 1. It should be noted that

Case	Radius, R_0 (μm)	Excitation frequency, f (kHz)	Captive/pendent bubble
1	232–253	2.422	Captive
2(*a*)	235–244	2.129	Captive
2(*b*)	260–266	0.5698	Captive
3	224–236	1.188	Captive
4	267–274	8.658	Captive
5	243–259	5.841	Captive
6	230–238	4.145	Pendent
7	202–250	11.21–12.94	Captive

TABLE 1. Summary of experimental cases.

during the course of the experiment, the bubbles grow slightly as a result of gas in the surrounding water diffusing into the bubble. The total growth in radius is usually ∼4 % of the bubble's initial radius.

4.1. *Case 1: a translating oscillation along a single axis*

The first mode of oscillation studied was a captive bubble undergoing a harmonic translating oscillation along a single axis. This mode of oscillation was excited at an acoustic frequency of 2.422 kHz and pressure amplitude of 34.05 Pa. The streak photographs and micro-PIV measured velocity fields along the various focal planes (§ 2.4.2) are shown in figure 7. Along the z_1-plane, the streaming flow pattern contains four vortices located roughly $2R_0$ from the centre of the bubble in a 'quadrupole' arrangement. Fluid moves towards the bubble along the horizontal axis and away from the bubble along the vertical axis of oscillation. There does not appear to be a significant local divergence in the flow field along this plane, i.e. it does not appear to have a significant z-component in the velocity. This appears to be a common feature in all the streaming flows observed along the z_1-plane. Presumably this effect is the result of a suppression in the depthwise component of flow caused by the plane wall boundary at the base of the bubble. The micro-PIV measured velocity field is not well resolved near the surface of the bubble. Continuous light micro-PIV has limitations in its temporal resolution, and therefore has difficulty in measuring the higher velocities typically observed near the surface of bubbles. This limitation affects the micro-PIV measured velocities in later cases as well. The maximum streaming velocities are approximately 0.3–0.35 mm s^{-1}.

The z_1-plane flow structure is significantly altered along the z_2- and z_3-planes with a greater degree of three-dimensional flow, particularly near the surface of the bubble. By traversing the focal plane along the z-axis, it appeared that fluid along these planes was drawn from near the plane wall from two source-like points shown near the top and bottom of the image along the axis of oscillation (y-axis). The fluid then moves towards the wall along two sink-like points opposite one another along the horizontal x-axis. These sink and source-like points are more clearly resolved along the z_3-plane. The in-plane velocities along this plane are ∼0.1 mm s^{-1}.

When we compare this streaming flow pattern with those of analytical solutions for a spherical bubble in an infinite domain (Davidson & Riley 1971; Longuet-Higgins 1998), there is some qualitative similarity, particularly along the z_1-plane. However, there are a few important differences. First, away from the base of the bubble, there is significant three-dimensional flow, whereas the streamlines predicted by theory are axisymmetric. This is a consequence of the hemispherical shape of the bubble and the

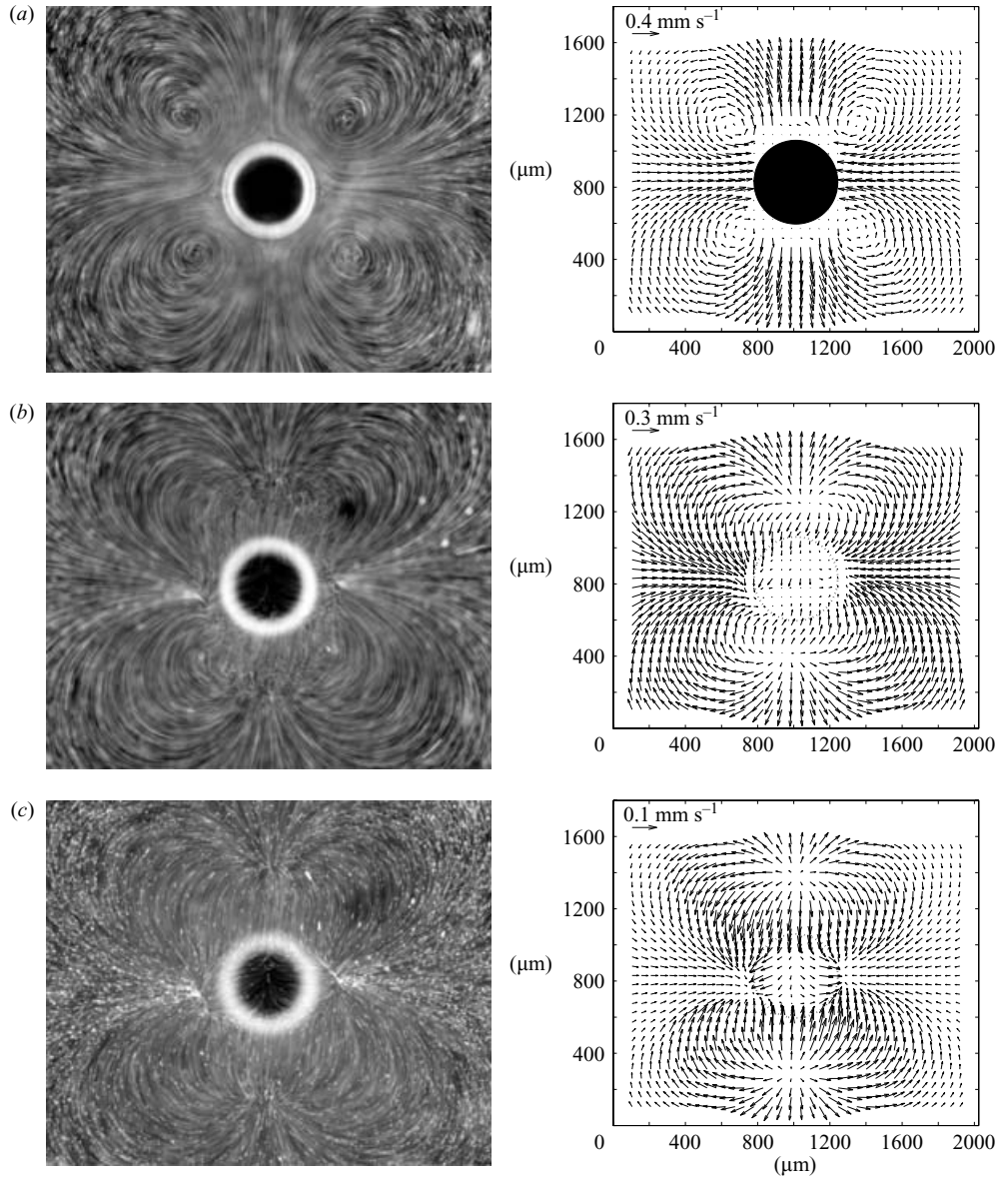

FIGURE 7. Case 1: a translating oscillation along a single axis. Streak photograph and micro-PIV velocity field along the (*a*) z_1-, (*b*) z_2- and (*c*) z_3-planes.

presence of the wall. The streamlines along the z_1-plane are also closed, whereas the streamlines of the theoretical solutions extend to infinity. This is a consequence of the bounded domain of the fluid in the microchamber. The most significant difference is that the streaming flow observed in these experiments moves in the opposite direction to what is theoretically predicted where fluid moves toward the bubble along the axis of oscillation. However, the direction of flow that we observe here does match the streamlines predicted by theory for the analogous cylinder and sphere where fluid moves away from the body along its axis of oscillation (Riley 1966, 1975). This would suggest that the boundary conditions on these bubbles are more like those of

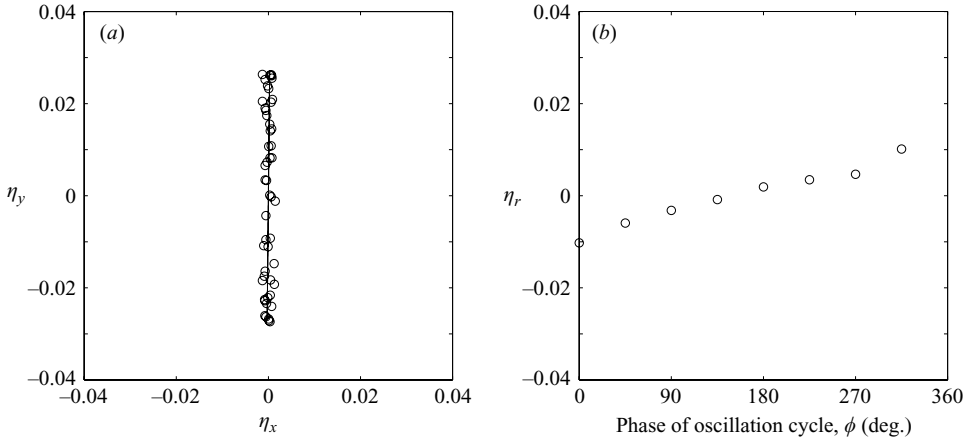

FIGURE 8. Case 1: a translating oscillation along a single axis. (*a*) Map of the bubble centroid positions η_x and η_y. (*b*) Variation in the bubble radius η_r over one cycle.

a rigid body. As was alluded to in § 3.1, this may be caused by a surface skin on the bubble. Another possibility is that the particles themselves have a 'no-slip' boundary, therefore any particles on the air–water interface will create a local 'no-slip' condition. Furthermore, being a hydrophobic polymer, the particles would rapidly tend to collect on the interface owing to the circulating fluid, increasing this effect.

If a surface skin on the bubble wall is indeed present, then there should also be four inner circulations within the Stokes layer as shown by Holtsmark *et al.* (1954) and Riley (1966). This Stokes layer circulation could not be detected in either the streak photographs or micro-PIV measurements. The thickness of the Stokes layer can be estimated as $(\nu/\omega)^{1/2}$, where ν is the fluid kinematic viscosity and ω is the angular oscillation frequency. Under the present experimental conditions, the Stokes layer is approximately 11–12 μm thick which would only be imaged over 6–7 pixels, which was too small to observe.

Figure 8(*a*) shows a plot of the motion of the centroid of the bubble along the focal plane, and verifies that the translating movements take place along the vertical axis of the image. While the centroid of the bubble is translating, the bubble remains attached to the chamber wall and thus its movement is more akin to a swaying motion than to a rigid-body translation. The data points on the graph were curve fitted using a least-squares method with the equations

$$\eta_x = a_x \sin(\theta) + x_0, \tag{4.1a}$$

$$\eta_y = a_y \sin(\theta) + y_0, \tag{4.1b}$$

where x_0 and y_0 are the non-dimensional equilibrium centroid coordinates, a_x and a_y are the amplitudes of oscillation in the x- and y-directions and $0 \leqslant \theta \leqslant 2\pi$. The amplitude of oscillation was found to be roughly 4–5 pixels over a bubble radius of 169 pixels. The curve fits allow the displacement amplitude to be measured to a subpixel accuracy of 2.67 % of the bubble's equilibrium radius. The standard deviations of the curve fitted centroid data in the x- and y-directions, given as σ_x and σ_y, respectively, were found to be less than 4.2 % and 1.5 % of the amplitude of oscillation in the y-direction. The amplitude of oscillation can also be used to determine the non-dimensional streaming parameters described in § 1. For this experiment, these values are $\epsilon = 2.67 \times 10^{-2}$, $M^2 = 816$ and $R_s = 0.58$.

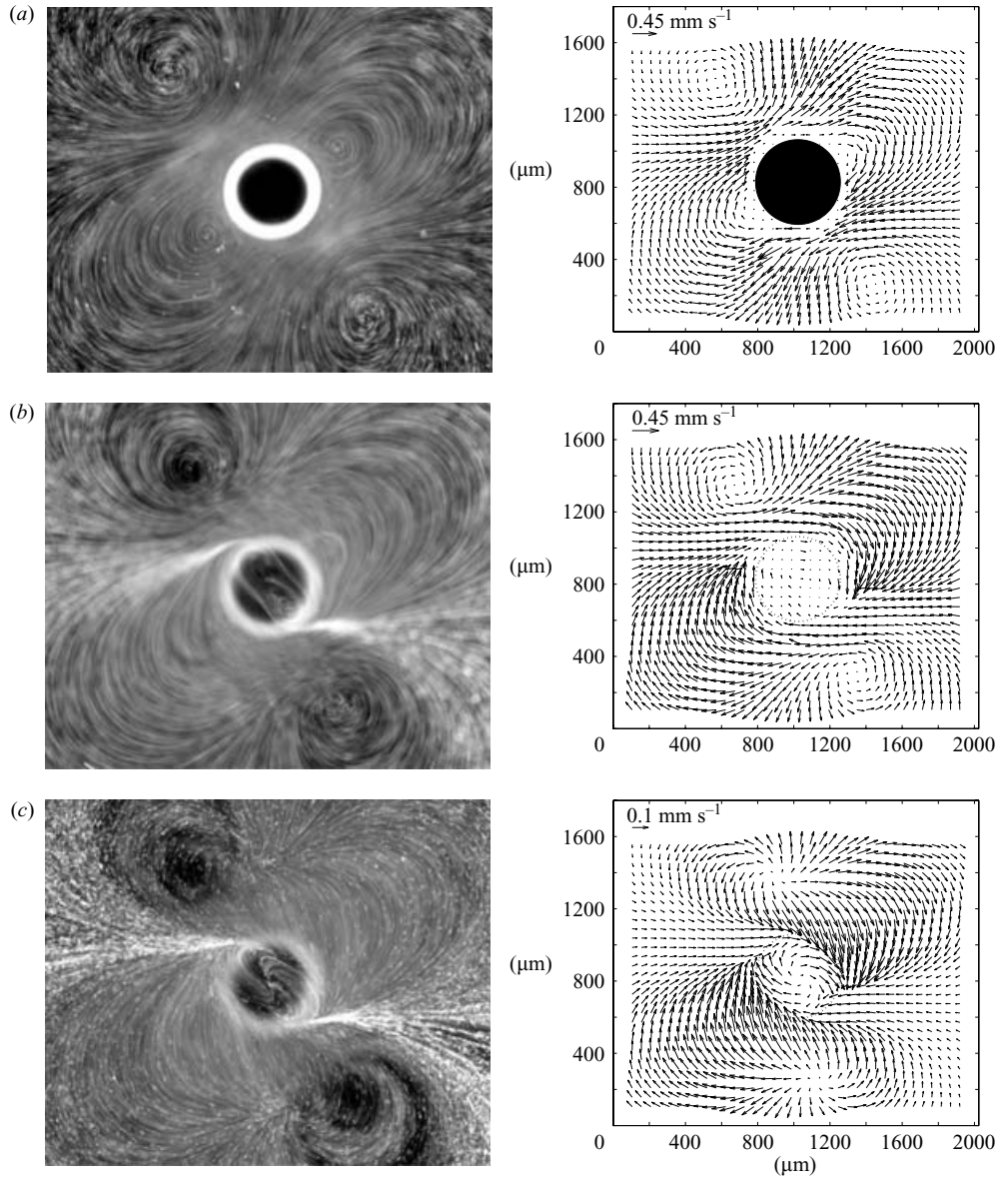

FIGURE 9. Case 2(a): an elliptical orbiting oscillation. Streak photograph and micro-PIV velocity field along the (a) z_1-, (b) z_2- and (c) z_3-planes.

Figure 8(b) is a plot of the variation in the radius of the bubble determined from the phase locked images, which shows there is a slight uniform increase in the size of the bubble's radius of about 1 % over one oscillation cycle. Similar observations are found in all other pure translating modes of oscillation (Cases 2a, 2b, 3 and 6). However, we attribute this to the diffusion of gas into the bubble over the course of the phase locked imaging rather than to a volume oscillating mode.

4.2. *Case 2(a): an elliptical orbiting oscillation*

A captive bubble underwent an elliptical orbiting motion along the focal plane at an acoustic frequency of 2.129 kHz and pressure amplitude of 14.30 Pa. Figure 9

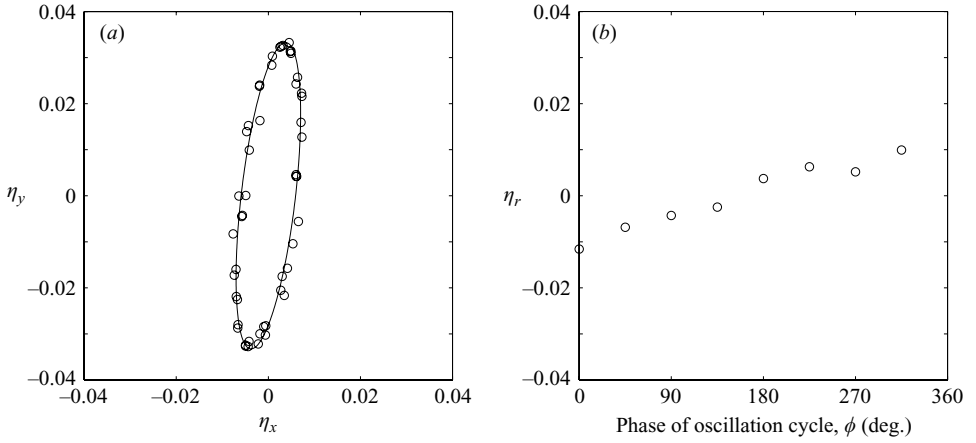

FIGURE 10. Case 2(a): an elliptical orbiting oscillation. (a) Map of the bubble centroid positions η_x and η_y. (b) Variation in the bubble radius η_r over one cycle.

shows the streak photographs and micro-PIV velocity fields. Along the z_1-plane, the streaming flow pattern resembles that of the linear translating bubble except the pattern appears skewed rather than orthogonal. Two vortices rotating with a clockwise sense are located near the surface of the bubble at $r = 1.5R_0$, while two outer vortices rotating with the opposite sense are located at roughly $r = 3.2R_0$. The streaming velocities are highest near the surface of the bubble and are approximately $0.45\,\mathrm{mm\,s^{-1}}$ in magnitude. The Stokes layer was too small ($\delta = 12.25\,\mu\mathrm{m}$ or 7–8 pixels) to detect visually the presence of any inner circulations. Along the z_2-plane, the two inner vortex structures are no longer apparent. However, near the top of the bubble, there appear two small vortices that are on a coincident line with the two outer vortices. The flow along the z_3-plane has similarities with the flow along the same plane for the linear translating bubble. There again appear to be two source-like points along the vertical axis with fluid moving out from these points toward an elliptical flow structure near the bubble's centre. The elliptical flow structure resembles an unstable focus centred along the bubble's primary axis. Along the edge of this elliptical structure, the flow moves out of the focal plane towards the wall the bubble is attached to. It is not clear whether the fluid from the centre of the focus is drawn from above or below this plane.

Figure 10(a) shows a plot of the centroid positions of the bubble along with curve fitted lines of the data points. The curve fits follow the equations

$$\eta_x = a_x \cos + x_0(\theta), \tag{4.2a}$$

$$\eta_y = a_y \sin + y_0(\theta), . \tag{4.2b}$$

A rotation transformation has also been applied to the ellipse to give the correct orientation.

The sense of the bubble's elliptical motion is clockwise, the same sense as the rotation of the two inner vortices surrounding the bubble. The minor to major axis ratio λ of the ellipse was found to be 0.176 and the ellipse was slightly rotated by an angle of 7° from the vertical axis. The maximum displacements of the centroid's position from their equilibrium, ϵ_x and ϵ_y, are roughly 0.588 % and 3.35 % of the bubble's equilibrium radius, respectively. The standard deviation of the data is roughly 10 % and 0.53 % of the minor and major axis, respectively. The standard deviation relative to the minor

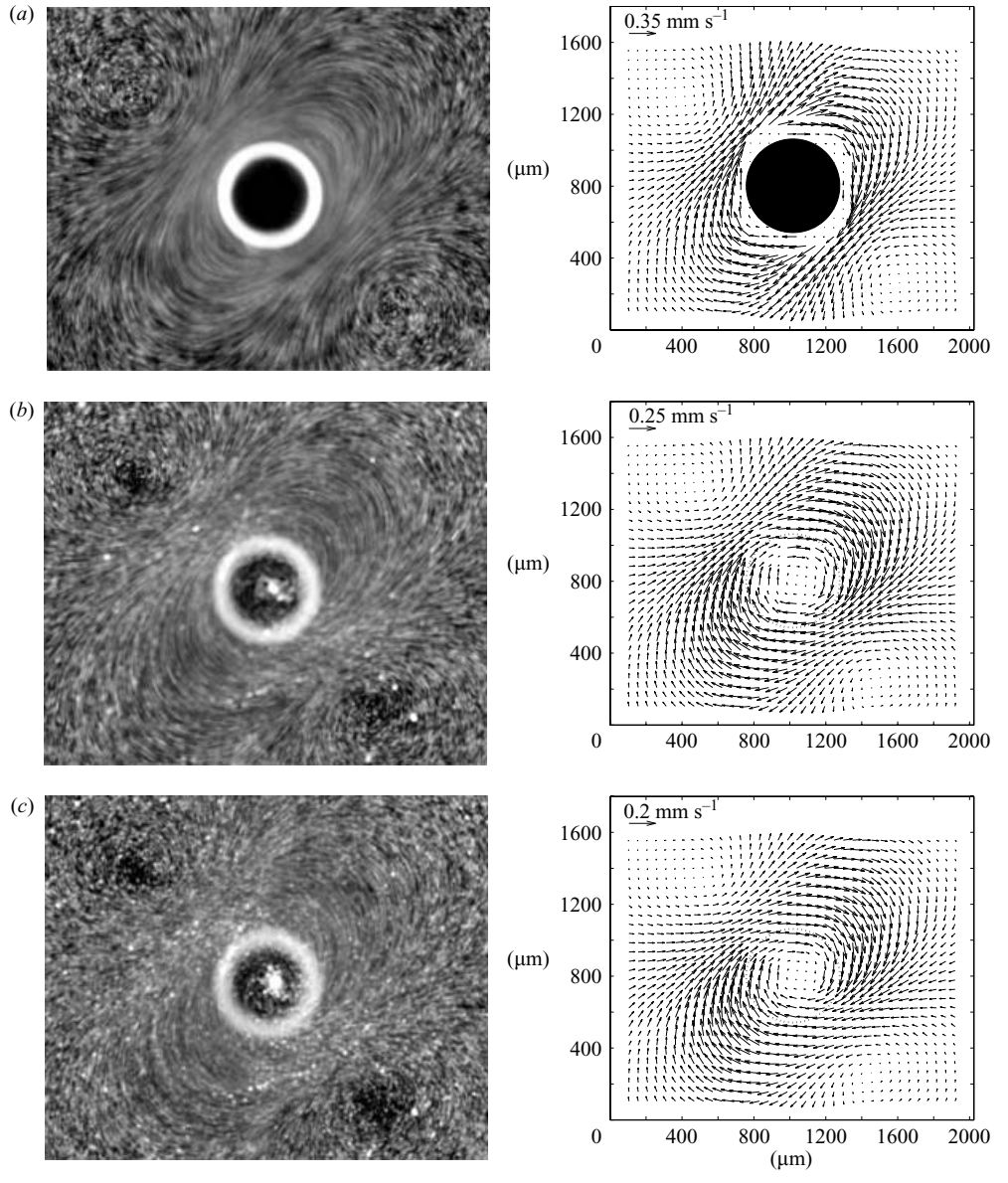

FIGURE 11. Case 2(b): an elliptical orbiting oscillation. Streak photograph and micro-PIV velocity field along the (a) z_1-, (b) z_2- and (c) z_3-planes.

axis is significant and thus its effect on the axis ratio λ is also significant. The non-dimensional streaming parameters of this case are $\epsilon_x = 5.88 \times 10^{-3}$, $\epsilon_y = 3.35 \times 10^{-2}$, $M^2 = 736$, $R_s, x = 2.54 \times 10^{-2}$ and $R_s, y = 8.24 \times 10^{-1}$. Figure 10($b$) is a plot of the variation in the bubble's radius and shows a similar result to Case 1.

4.3. *Case 2(b): an elliptical orbiting oscillation*

The bubble studied in this section undergoes a similar elliptical orbit to the previous section; however, the streaming pattern is slightly altered. This orbiting motion was induced at an acoustic excitation frequency of 569.8 Hz. The streak photograph and velocity fields of this bubble are shown in figure 11 for an acoustic pressure amplitude

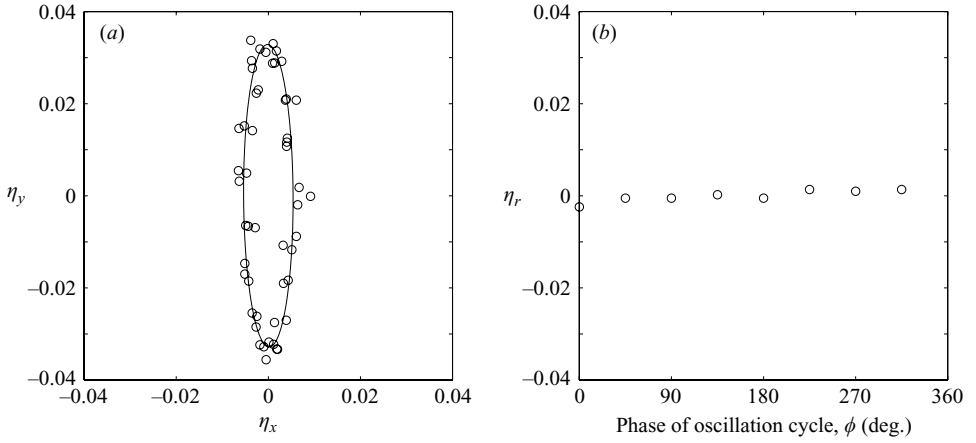

FIGURE 12. Case 2(*b*): an elliptical orbiting oscillation. (*a*) Map of the bubble centroid positions η_x and η_y. (*b*) Variation in the bubble radius η_r over one cycle.

of 23.80 Pa. Along the z_1-plane, the streaming flow pattern appears almost identical to the previous case except that the flow field no longer contains the two inner vortices near the bubble. The motion in the vicinity of the bubble can be described by elliptical streamlines going around the bubble. The two outer vortices are still present and are located at a distance of roughly $r = 3R_0$ and rotate in an anticlockwise direction. The streaming velocities are highest near the surface of the bubble ($\sim$0.325 mm s^{-1}) and decrease with radial distance.

Flow along the z_2- and z_3-planes is similar to that along the z_1-plane with maximum streaming velocities of approximately 0.2 mm s^{-1}. Directly above the bubble, the flow resembles a stable focus that moves towards the axis that passes through the bubble's centre.

Figure 12(*a*) shows the map of centroid positions the bubble moves through, which is clearly an elliptical orbit. The motion of the ellipse is clockwise; the same direction as the elliptical streamlines surrounding the bubble. The axis ratio of the ellipse is similar to the previous elliptical orbiting bubble with an axis ratio of $\lambda = 0.164$. The amplitude of oscillation of this elliptical orbit is also similar to the previous case. From the curve fitted equations, the minor and major axes of the ellipse are roughly 0.537 % and 3.28 % of the bubble's equilibrium radius, respectively. The standard deviations of the curve fits are roughly 21 % of the minor axis and 1.7 % of the major axis. As was the case with the first elliptical orbiting oscillation, the standard deviation of the data is significant in the minor axis direction. The oscillatory motion of the bubble results in a similar streaming regime to the other modes of oscillation, i.e. $\epsilon_x = 5.37 \times 10^{-3}$, $\epsilon_y = 3.28 \times 10^{-2}$, $M^2 = 241$, $R_s, x = 6.96 \times 10^{-3}$ and $R_s, y = 2.60 \times 10^{-1}$. Also, a plot of the variation in the bubble's radius over one cycle confirms the mode of oscillation is purely translational (figure 12*b*).

4.4. *Case 3: a circular orbiting oscillation*

The streaming flow around a captive bubble which undergoes a small-amplitude anticlockwise circular orbit was induced at an acoustic frequency of 1.188 kHz and a pressure amplitude of 46.20 Pa. The streamlines and velocity fields around the bubble are shown in figure 13. The z_1- and z_2-planes show an anticlockwise circular vortex centred on the bubble with velocities of approximately 0.45 mm s^{-1}. The velocities at the surface of the bubble should be higher and are not properly measured by this

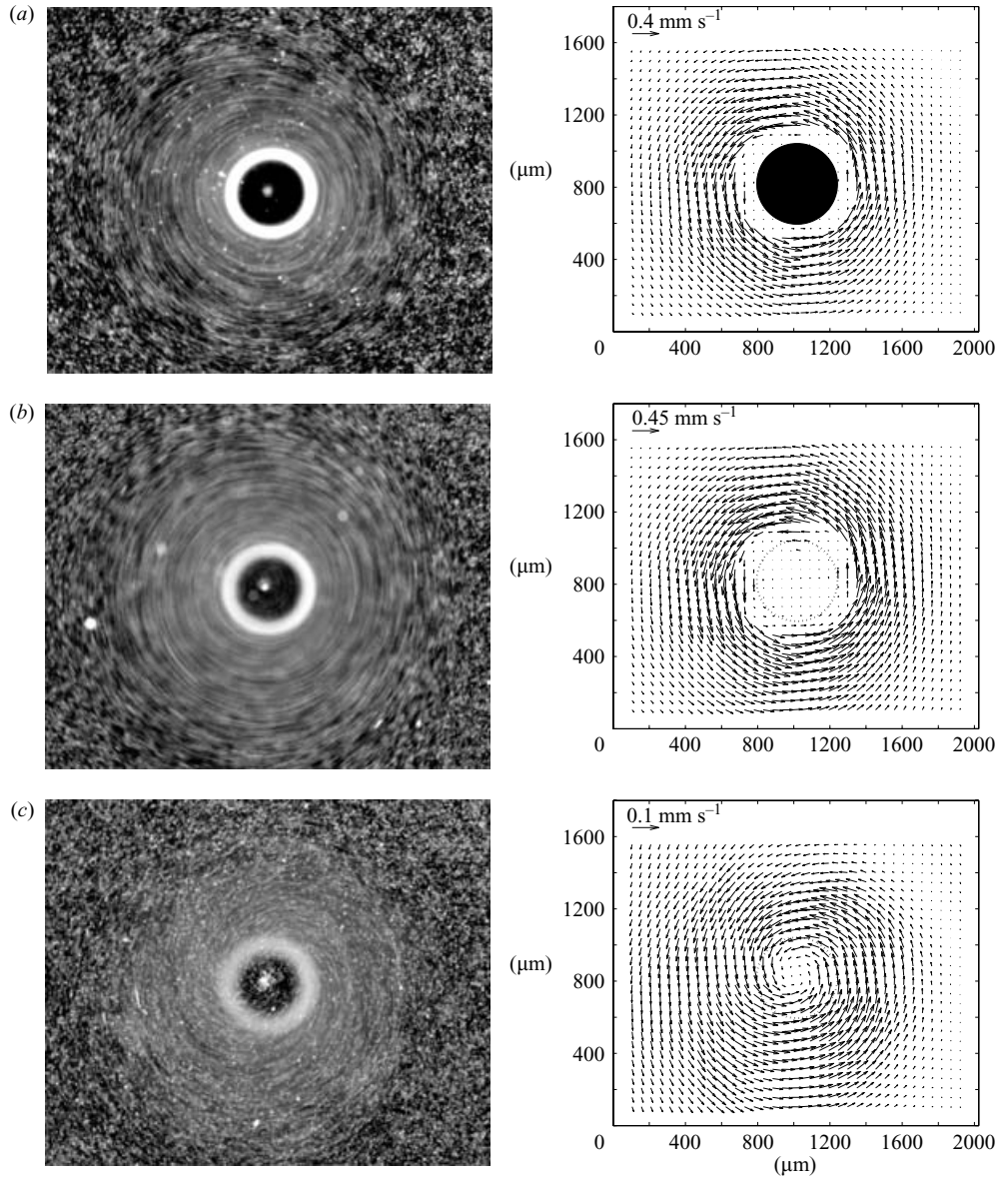

FIGURE 13. Case 3: a circular orbiting oscillation. Streak photograph and micro-PIV velocity field along the (*a*) z_1-, (*b*) z_2- and (*c*) z_3-planes.

micro-PIV system. Along the z_3-plane, the flow resembles a swirling vortex with fluid moving towards a stable focus-like point centred over the bubble.

Although this mode of oscillation has not been observed or modelled before for a bubble, it has been theoretically modelled for the analogous cylinder and sphere. Riley (1971) studied the streaming around a cylinder which undergoes a small-amplitude circular orbit and showed the Stokes-layer solution matches directly with the potential vortex solution. Lee & Wang (1989) studied this mode of oscillation for a rigid sphere. They showed that the streaming directly adjacent to the surface of the sphere is a swirling vortex moving towards the poles of the sphere, while directly outside the

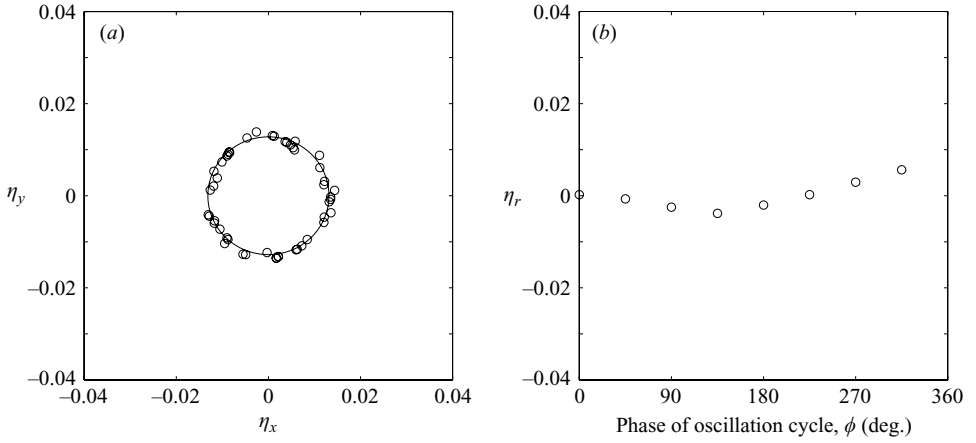

FIGURE 14. Case 3: a circular orbiting oscillation. (*a*) Map of the bubble centroid positions η_x and η_y. (*b*) Variation in the bubble radius η_r over one cycle.

boundary layer, fluid moves outward from the poles of the sphere to the equator. In Lee & Wang's solutions, the outer streaming appears to move in the opposite direction to that observed in the present experiment. This observation seems to contradict the idea that the bubbles have a boundary condition like that of a rigid body and it is uncertain whether or not the boundary condition of the bubble is a 'free-slip' condition. The development of a model for this mode of oscillation would be helpful in answering these questions.

The map of the centroid path traced out by the bubble is shown in figure 14(*a*) and shows a circular orbit moving in an anticlockwise direction with an axis ratio of $\lambda = 0.973$. The orbital radius is approximately 1.3 % of the bubble's equilibrium radius which corresponds to streaming parameters of $\epsilon_x = 1.31\times10^{-2}$, $\epsilon_y = 1.28\times10^{-2}$ $M^2 = 373$, $R_s, x = 6.45 \times 10^{-2}$ and $R_s, y = 6.10 \times 10^{-2}$. Also, figure 14(*b*) shows the bubble is not undergoing any significant volume oscillation.

We can compare Cases 1–3 together if we consider them as general elliptical orbiting oscillations with Case 1 corresponding to the minor axis equal to zero ($\lambda = 0$) and Case 3 corresponding to equal major and minor axes ($\lambda = 1$). Elliptical orbiting oscillations of a bubble have been studied neither experimentally nor theoretically; however, Riley (1992) studied the streaming around a cylinder when two orthogonal plane sound waves were incident on it. The plane sound waves were of the same frequency, with a phase difference of $\pi/2$ and a difference in the amplitude factor of λ. This problem is equivalent to a cylinder that moves along an elliptical path with an axis ratio of λ. The limiting case of $\lambda = 1$ was found to be a Stokes-layer solution matching a potential vortex, whereas for the other case of $\lambda = 0$, Davidson & Riley (1972) conjectured that boundary layers in the outer flow would collide, forming jet-like flows erupting from the cylinder surface. For intermediate values of λ, Riley conjectures a critical value of the axis ratio λ_c in which, for $\lambda_c < \lambda \leqslant 1$, the flow within the outer boundary layer is circulatory, whereas for $0 \leqslant \lambda \leqslant \lambda_c$, jet-like structures are formed.

In the present experiments, a critical axis ratio for elliptical orbiting bubbles appears to exist as well. This observation is based on how the streaming patterns transform between one another. The streaming flows in Cases 1–3 transition between one another in a smooth and orderly sequence as the frequency is monotonically

increased or decreased. This may occur in the following manner: the streaming flow may begin as Case 1 with the streaming flow containing four vortices surrounding the bubble. Then, as the frequency is increased, this pattern becomes skewed. As the frequency is increased further, the two inner vortices disappear and are replaced by elliptical streamlines surrounding the bubble and finally the outer vortices are also lost and the flow is a uniform circulation around the bubble. This sequence would suggest that the elliptical orbits of the bubble also transform smoothly from a linear translation, to an elliptical orbit and finally to a circular orbit. The difference in streaming patterns is then a result of a variation in λ.

We believe there is an important transition from Cases 2(a) to 2(b) where the flow structure appears almost identical except for the disappearance of the two inner vortices near the surface of the bubble. The experimental value of λ in Case 2(a) is slightly larger than that in Case 2(b) which appears to disagree with what would be expected if the above argument were true. The values of λ generally differ by only $\sim$6 % whereas the standard deviations of the curve fits relative to the minor axis are between 10 and 30 %. Unfortunately, these standard deviations of λ are significant and thus we cannot confirm whether the switch occurs at a λ value consistent with the above argument. Riley's study of a cylinder undergoing an elliptical orbit suggested a critical value of $\lambda_c \approx 0.213$. In the present experiments, the transition for streaming patterns to change from Case 2(a) to Case 2(b) appears to occur between $\lambda_c = 0.156$–0.186. This value of λ_c also uses values of λ determined from experiments performed at several other pressure amplitudes.

4.5. *Case 4: a volume oscillation*

The preceding modes of oscillation have been purely translating modes of oscillation. Here, a captive bubble was excited into a volume oscillation at an acoustic excitation frequency of 8.658 kHz which is below the estimated natural frequency (12.3 kHz) based on (1.1). The streaming flow field and velocity measurements along the three focal planes are shown in figure 15 for an acoustic pressure amplitude of 225.32 Pa. The streaming flow pattern is clearly directional with a plane of symmetry along the vertical axis. The fluid moves downward from the top of the image and is recirculated back to the top again within the symmetric halves of the image. Near the surface of the bubble, the fluid moves up and over the surface of the bubble to the other side with fluid velocities of approximately 0.3 mm s^{-1}. The streaming flow resembles a 'dipole' structure.

The streaming flow observed here may be compared with the streamlines modelled by Wu & Du (1997) of a spherical bubble undergoing a volume oscillation due to a propagating sound wave. The streamlines determined by Wu & Du show fluid moving along the axis of the propagating sound wave which is similarly observed in this experiment. However, their solution depicts streamlines that are axisymmetric and there are no closed streamlines. These observations are a consequence of the hemispherical shape of the bubble and the enclosed environment rather than free-field conditions assumed in the model. Also the direction of streaming in the experiments suggests that the sound waves incident on the bubble travel along the vertical axis of the image. This is to be expected as the piezoelectric disk is positioned along the y-axis and directly above the top of the image, so that any acoustic wave it generates would most probably move in this direction.

A plot of the centroid positions of the bubble is shown in figure 16(a) and shows that the x- and y-components of the bubble's motion remain mostly fixed in position, although there is a small perturbation along the y-direction. This small component

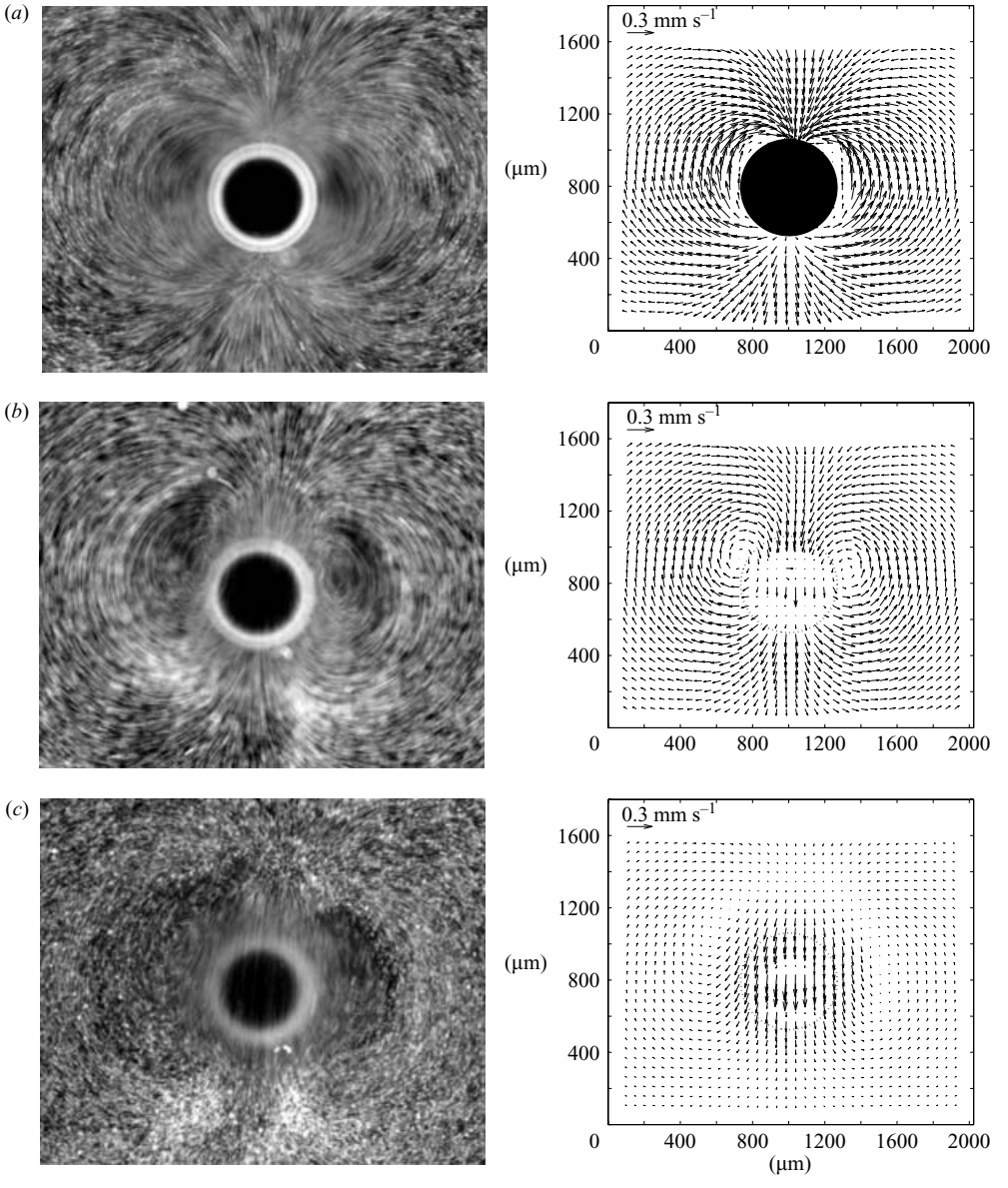

FIGURE 15. Case 4: a volume oscillation. Streak photograph and micro-PIV velocity field along the (*a*) z_1-, (*b*) z_2- and (*c*) z_3-planes.

in oscillatory motion may be responsible for the directionality of the flow field. Figure 16(*b*) shows the variation in the bubble's radius over one cycle. The data show that the radius varies sinusoidally with the same frequency as the excitation signal. The lag in phase between the excitation signal and the volume oscillation is about 110°. The bubble's radius data were fitted with a sinusoidal curve fit described by

$$\eta_r = a_r \sin(\theta + b_r) + c_r, \tag{4.3}$$

where a_r represents the amplitude of radius oscillation, b_r is the phase of the oscillation relative to the excitation signal, c_r is the average change in radius over one cycle and

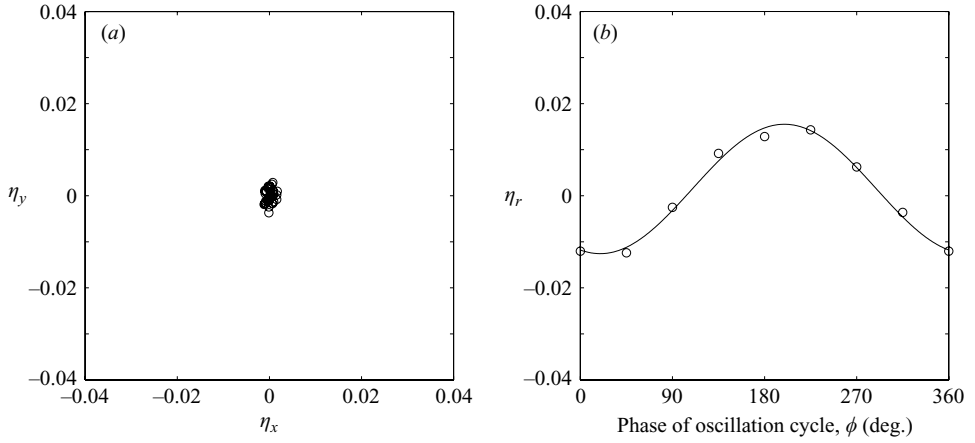

FIGURE 16. Case 4: a volume oscillation. (*a*) Map of the bubble centroid positions η_x and η_y. (*b*) Variation in the bubble radius η_r over one cycle.

$0 \leqslant \theta \leqslant 2\pi$. The amplitude of radius oscillation, a_r, is roughly 1.41 % of the bubble's equilibrium radius.

4.6. *Case 5: a translating and volume oscillation*

The case studied in this section involves a captive bubble undergoing a translating oscillation along a single axis and a simultaneous volume oscillation. This mode of oscillation was excited at an acoustic frequency of 5.841 kHz and a pressure amplitude of 14.18 Pa. The streak photographs and micro-PIV velocity field measurements are shown in figure 17. The streaming flow pattern is similar to the pure volume oscillating bubble in that there is a plane of symmetry with flow being recirculated from one end of the bubble to the other. However, the cores of the circulations appear to have been shifted away from the bubble. This is more apparent along the z_2-plane where the two vortices can be observed on either side of the bubble. The addition of a translating oscillation mode appears to modify the flow pattern, although the same basic 'dipole' flow structure remains. This point was also mentioned by Wu & Du (1997) who state that the streaming induced by the volume oscillating mode will dominate over translating modes. The flow field predicted by Longuet-Higgins (1998) of a bubble undergoing this mode of oscillation, shares some similarities with the flow pattern observed here. The differences in the lack of axisymmetry and closed streamlines can again be explained by the hemispherical shape of the bubble and the boundary walls of the system.

Figure 18(*a*) shows a map of the bubble's centroid positions and indicates that the amplitude of the translating oscillation along the vertical axis is roughly 0.6 % of the equilibrium radius. The variation in the bubble's radius over one cycle is shown in figure 18(*b*) and indicates the radius is oscillating sinusoidally with the same frequency as the excitation signal. At an acoustic pressure amplitude of 14.18 Pa, the radius oscillates with an amplitude of roughly 1.64 % of the bubble's equilibrium radius.

4.7. *Case 6: a translating oscillation along an axis perpendicular to the wall*

The bubble studied in this section is a pendent bubble undergoing what appears to be a translating oscillation along the axis perpendicular to the wall the bubble is attached to (z-axis). The bubble was driven into oscillation by an acoustic frequency

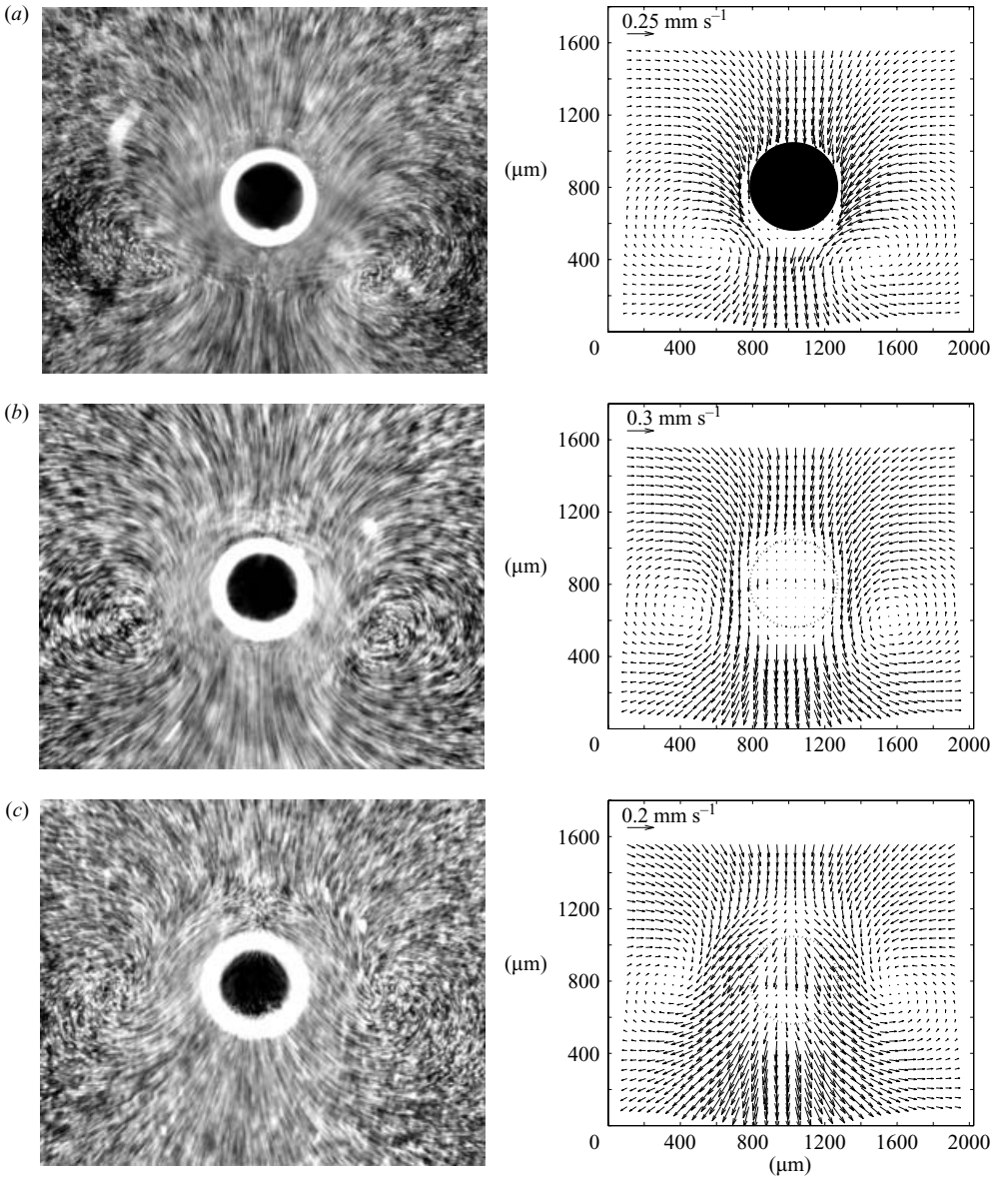

FIGURE 17. Case 5: a translating and volume oscillation. Streak photograph and micro-PIV velocity field along the (*a*) z_1-, (*b*) z_2- and (*c*) z_3-planes.

of 4.145 kHz and pressure amplitude of 30.06 Pa. The streak photograph and velocity field measurements for the various planes are shown in figure 19. Along the z_1- and z_2-planes, fluid moves radially inward towards the bubble. Near the bubble there is necessarily a z-component in the flow where fluid begins to move away from the plane wall. The fluid is pushed up and flows radially outward along the z_3-plane. The in-plane velocities are approximately 0.1–0.2 mm s^{-1} near the bubble and decrease with radial distance. The flow visualization suggests that the streaming flow around the bubble is a vortex ring with fluid drawn towards the bubble near the plane wall the bubble is attached to, and away from the bubble away from this wall. A similar mode

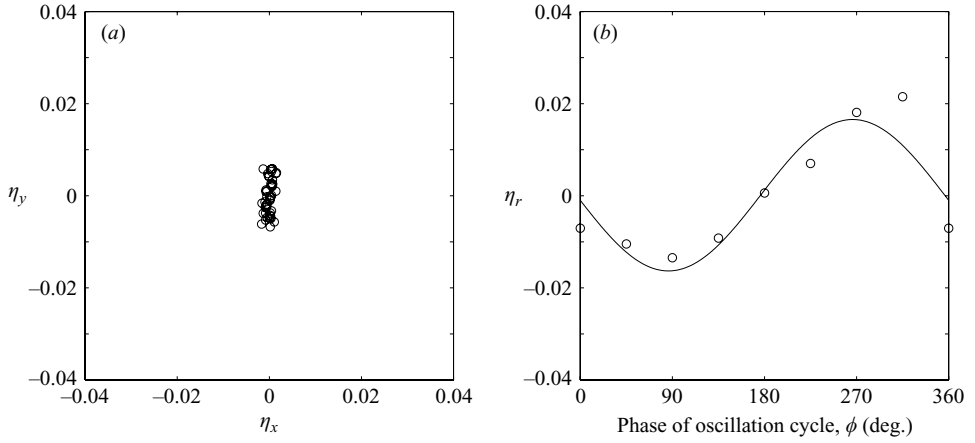

FIGURE 18. Case 5: a translating and volume oscillation. (*a*) Map of the bubble centroid positions η_x and η_y. (*b*) Variation in the bubble radius η_r over one cycle.

of oscillation has been studied experimentally by Elder (1959) and Marmottant & Hilgenfeldt (2003) where they induce volume oscillations on a pendent bubble resting on a solid boundary causing the centroid of the bubble to translate along an axis perpendicular to the wall. They also similarly observe a vortex ring around the bubble, although these rings are not confined between two plane walls adjacent to the bubble. The direction of the streaming we observe is in the same direction as Elder's bubble which has a surface skin, while opposite in direction to a clean bubble.

Measurement of the mode of oscillation of the bubble is difficult, given that the suggested oscillation occurs perpendicular to the imaging plane. A plot of the centroid positions (figure 20*a*) shows that there is little in-plane motion along these axes, while a plot of the variation in the bubble's radius over one cycle (figure 20*b*) shows the bubble is not undergoing a volume oscillation either. In fact, the acoustic excitation frequency is well below that of the natural frequency ($\sim$14.27 kHz), suggesting the most likely mode of oscillation of the bubble is a translation along the z-axis.

4.8. *Case 7: Shape mode oscillations*

The microstreaming flows around bubbles undergoing shape mode oscillations was briefly investigated. Shape mode oscillations distort the bubble from its usual spherical shape into various polygonal shapes depending on the particular shape mode n (Kornfeld & Suvorov 1944). Several different shape modes were observed. The streaming flow pattern was recorded using streak photography along the z_1-plane and a series of brightfield images were also taken to capture the basic features of the shape mode. However, there was difficulty in stabilizing a bubble in any particular mode of oscillation. The bubbles did not remain stable for very long, usually 15–30 s. Most often the bubble would change into another mode of oscillation (a volume or a different shape mode) or occasionally the bubble would detach from its fixed position and move around erratically. This erratic movement may be related to the 'dancing bubble' phenomenon observed in bubbles located in standing waves which also exhibit erratic movements when they develop surface instabilities (see Strasberg & Benjamin 1958; Eller & Crum 1970; Doinikov 2004). These issues made it difficult to carry out micro-PIV measurements and phase locked imaging of the bubble's mode of oscillation.

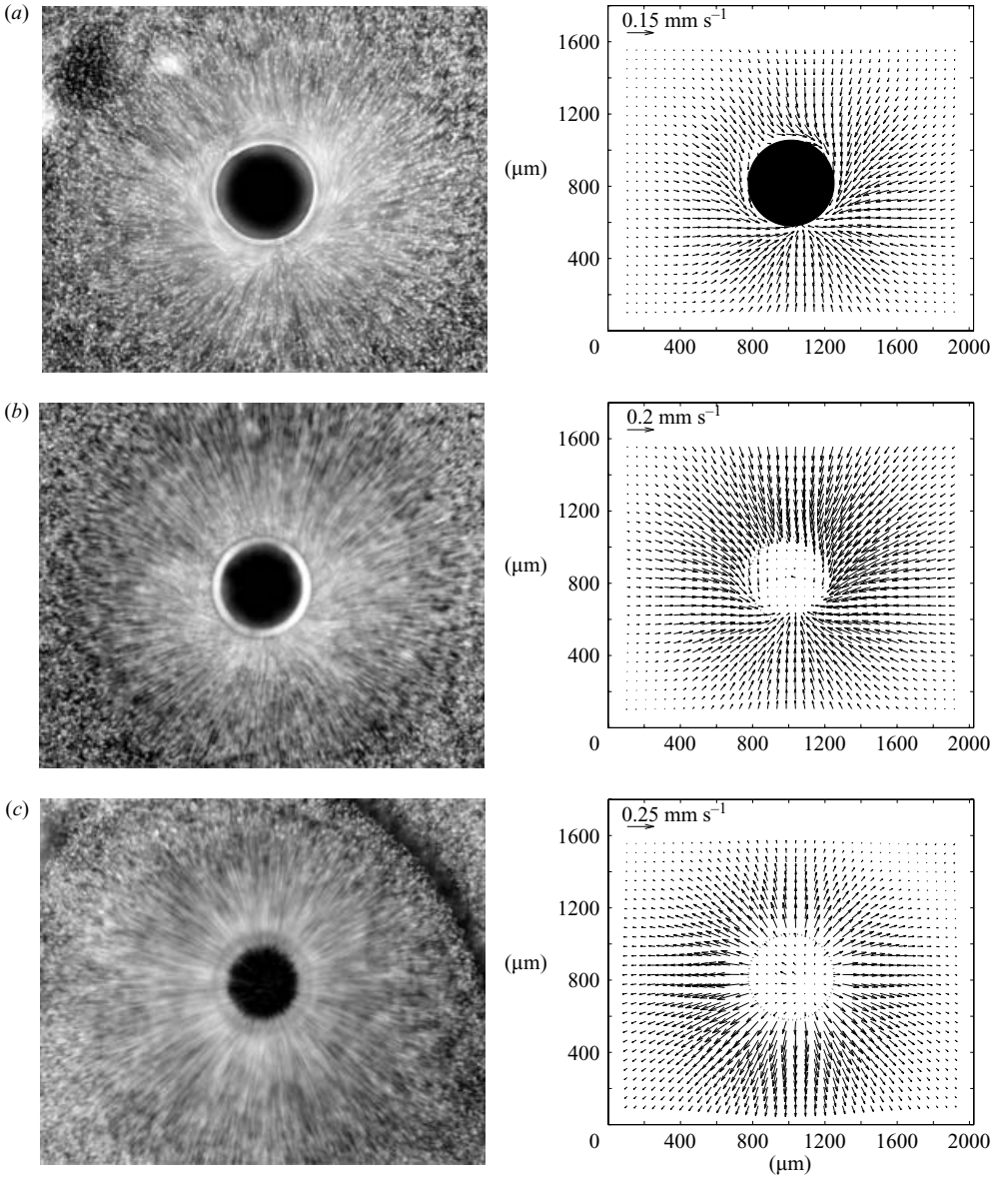

FIGURE 19. Case 6: a translating oscillation along an axis perpendicular to the wall. Streak photograph and micro-PIV velocity field along the (*a*) z_1-, (*b*) z_2- and (*c*) z_3-planes.

The shape mode oscillations occur in a small band of frequencies (10–12 kHz) and only when the voltage amplitude of the excitation signal was 30 V_{pp} or greater. Furthermore, the small band of frequencies in which the shape oscillations occur is also in the range near the resonance frequency of the piezoelectric disk. This suggests the oscillations are induced when a pressure threshold is overcome which implies they are the result of a parametric instability (see Eller & Crum 1970; Francescutto & Nabergoj 1978; Marston 1980). Directly above and below the frequency band in which shape oscillations occur, bubbles typically undergo the volume oscillating mode in which

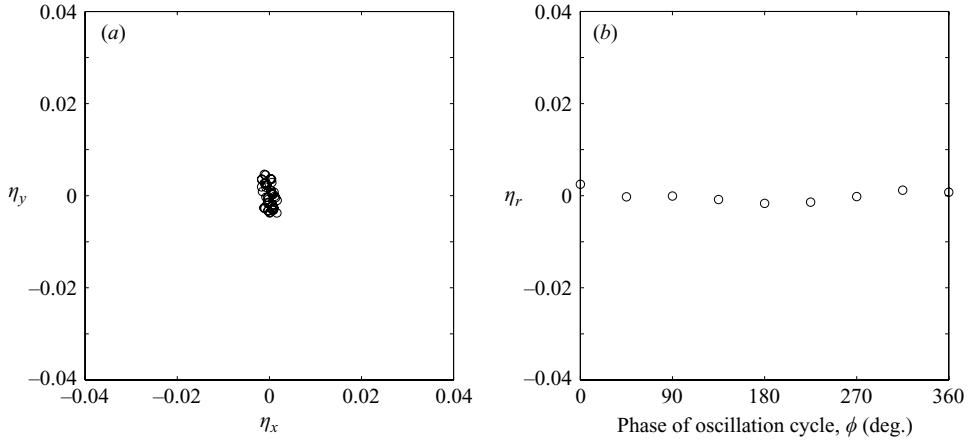

FIGURE 20. Case 6: a translating oscillation along an axis perpendicular to the wall. (*a*) Map of the bubble centroid positions η_x and η_y. (*b*) Variation in the bubble radius η_r over one cycle.

the characteristic 'dipole' streaming pattern (see § 4.5) is observed. Small adjustments in the frequency within this band result in different modes of oscillation evidenced by different bubble shapes or streaming patterns. The streaming velocities of shape mode oscillating bubbles appeared to be roughly 2–3 times higher than those found in volume and translating modes of oscillation. This result appears to agree with the observations made by Watson, Birkin & Leighton (2003) who observed the mass transfer enhancement in the vicinity of bubbles undergoing volume oscillations and also bubbles with surface waves. They measured the mass transfer of electrochemical species to a microelectrode and found that the transfer was higher in bubbles with surface waves compared to bubbles undergoing a volume oscillation. The authors reason this is because the amplitude of the displacement of the bubble's wall with surface waves ($\sim$75 μm) is a magnitude higher than the wall displacements due to the volume oscillation ($\sim$3 μm). Birkin *et al.* (2002) also studied the enhanced mass transfer around a captive bubble with Faraday waves on its surface and attribute this observation to the forced convection induced by the surface waves. However, neither Watson *et al.* nor Birkin *et al.* study the actual streaming flow patterns and do not appear to identify microstreaming as the driving mechanism for the convection. The streaming flows around bubbles with surface waves were also studied by Elder (1959), who observed vortex ring patterns around the bubbles. However, he does not identify the specific shape modes observed and it is uncertain whether the surface waves he observes are Faraday waves or shape mode oscillations. The streaming patterns for three different shape modes observed in our experiments are shown in figure 21. The bubble shapes suggest the presence of the $n = 6$, 7 and 8 modes.

4.9. *Effects of the pressure amplitude*

Cases 1–7 were all performed at an acoustic pressure amplitude corresponding to an excitation signal of 30 V_{pp} delivered to the piezoelectric disk. Experiments for Cases 1–6 were also performed at three other acoustic pressure amplitudes corresponding to voltage amplitudes of 15, 20 and 25 V_{pp}. The actual pressure delivered is a function of the frequency and voltage amplitude of the excitation signal, as indicated in figure 2.

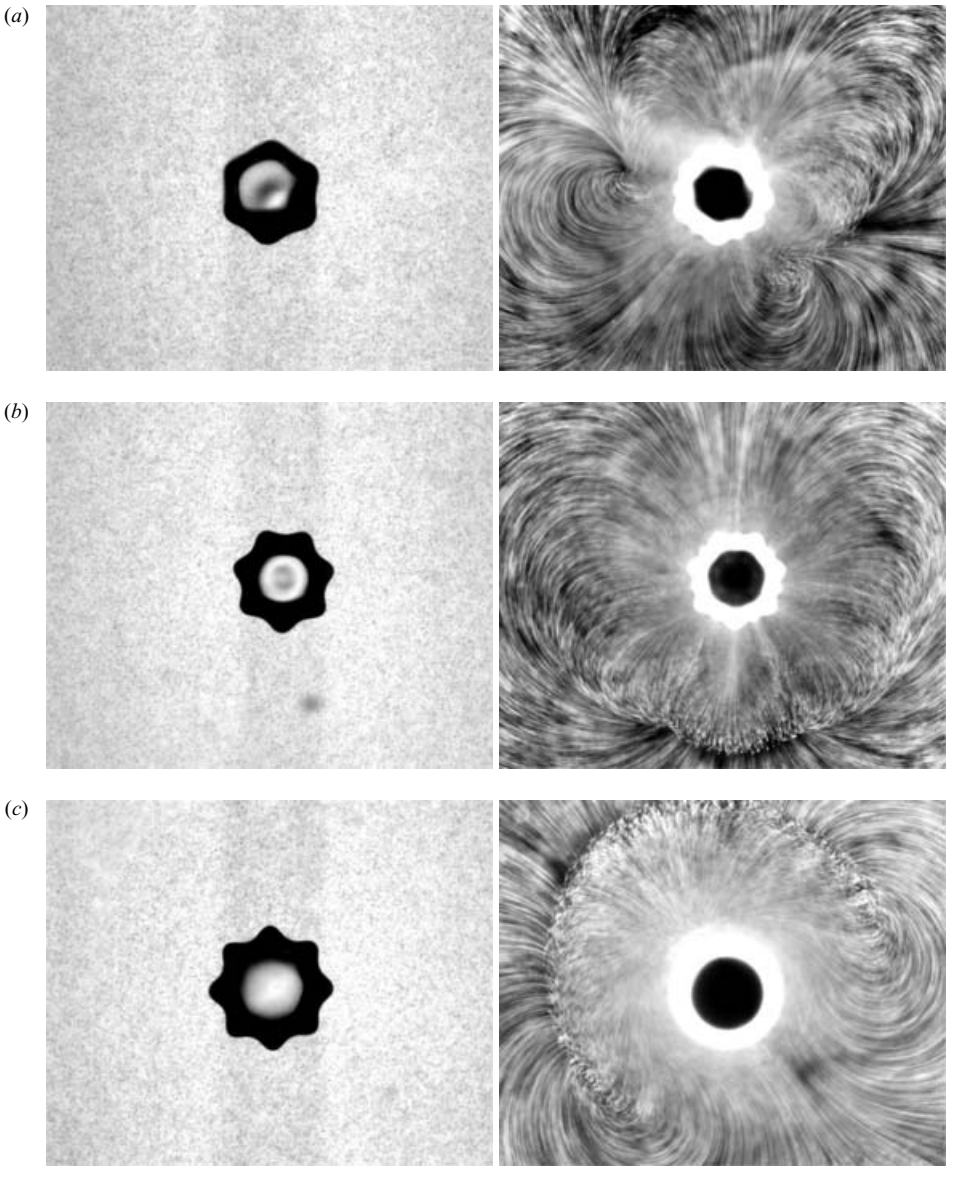

FIGURE 21. Case 7: shape mode oscillations. Brightfield image and streak photograph of (*a*) $n = 6$, (*b*) $n = 7$ and (*c*) $n = 8$ modes along the z_1-plane. Pictures on the left-hand side are taken using brightfield illumination and pictures on the right-hand side are taken using epifluorescent illumination.

There were a number of general observations found. It was observed that as the pressure amplitude increased in magnitude, and all other conditions held constant, the streaming velocities also increased, but generally the topology of the streaming flow pattern would remain unchanged. Plots of the bubble's primary oscillatory motion (centroid motion or volume oscillation) showed the amplitude of oscillation increased linearly with the pressure amplitude, but the form of the motion remain unchanged, e.g. an elliptical motion would retain the same axis ratio. The only exception to this

Bubble	ϵ	M^2	R_s
1	2.252×10^{-2}	637.6	3.234×10^{-1}
2	2.257×10^{-2}	607.9	3.098×10^{-1}

TABLE 2. Case A: two bubbles undergoing translating oscillations along single axes. Non-dimensional streaming parameters.

was when an increase in pressure amplitude induced a shape mode oscillation of the bubble.

5. Microstreaming around multiple bubbles

The microstreaming flow around a pair of bubbles undergoing three different modes of oscillation was briefly studied. All the experiments were carried out with a $30\,V_{pp}$ excitation signal and with all bubbles held in a captive position and placed adjacent to one another. In the following sections, the bubble shown on the left-hand side of the image will be referred to as 'Bubble 1' and on the right-hand side bubble as 'Bubble 2'.

5.1. *Case A: two bubbles undergoing translating oscillations along single axes*

Translating oscillations along single axes were induced in two bubbles at an acoustic frequency of 2.267 kHz and pressure amplitude of 18.61 Pa. Bubbles 1 and 2 have radii of 212 and 208 μm respectively. Figure 22 shows the streak photographs and micro-PIV velocity fields along the z_1-, z_2- and z_3-planes. The streaming flow patterns observed are what might be expected if one were to use a method of images on an individual bubble to give a mirror set of flow patterns. The vortices between the bubbles are squashed in appearance because of the presence of another bubble, and there are several saddle points along the plane of symmetry between the bubbles. The maximum streaming velocities are approximately $0.25\,mm\,s^{-1}$. The streaming flow pattern appears less symmetrical along the z_2- and z_3-planes as the bubbles are slightly mismatched in size.

The mode of oscillation of the two bubbles is shown in figure 23 where the vertical translation of the bubble has an amplitude of approximately 2.25 % of each bubble's equilibrium radius with a standard deviation of less than 3 % of this. The streaming parameters of the bubbles are summarized in table 2 and correspond to $\epsilon \ll 1$, $M^2 \gg 1$ and $R_s = O(1)$. The variation in the bubble's radius over one cycle shows a similar observation to the single bubble case in that there is a uniform increase in the bubble radius. However, as was noted earlier, this appears to be due to the growth of the bubble that occurs over the course of the experiment as a result of the diffusion of gas into the bubble.

5.2. *Case B: two bubbles undergoing elliptical orbiting oscillations*

Two bubbles underwent elliptical orbiting oscillations at an acoustic frequency of 1.381 kHz and pressure amplitude of 52.53 Pa. Bubbles 1 and 2 have radii of 207 μm and 215 μm, respectively. The streak photographs and velocity fields of the flow field are shown in figure 24. The streamlines around the bubble show an anticlockwise circulation around each bubble with a saddle point located between them. Fluid near the surface of the bubbles remain in circulation around each bubble, but fluid further away circulates around both bubbles. The maximum streaming velocities are

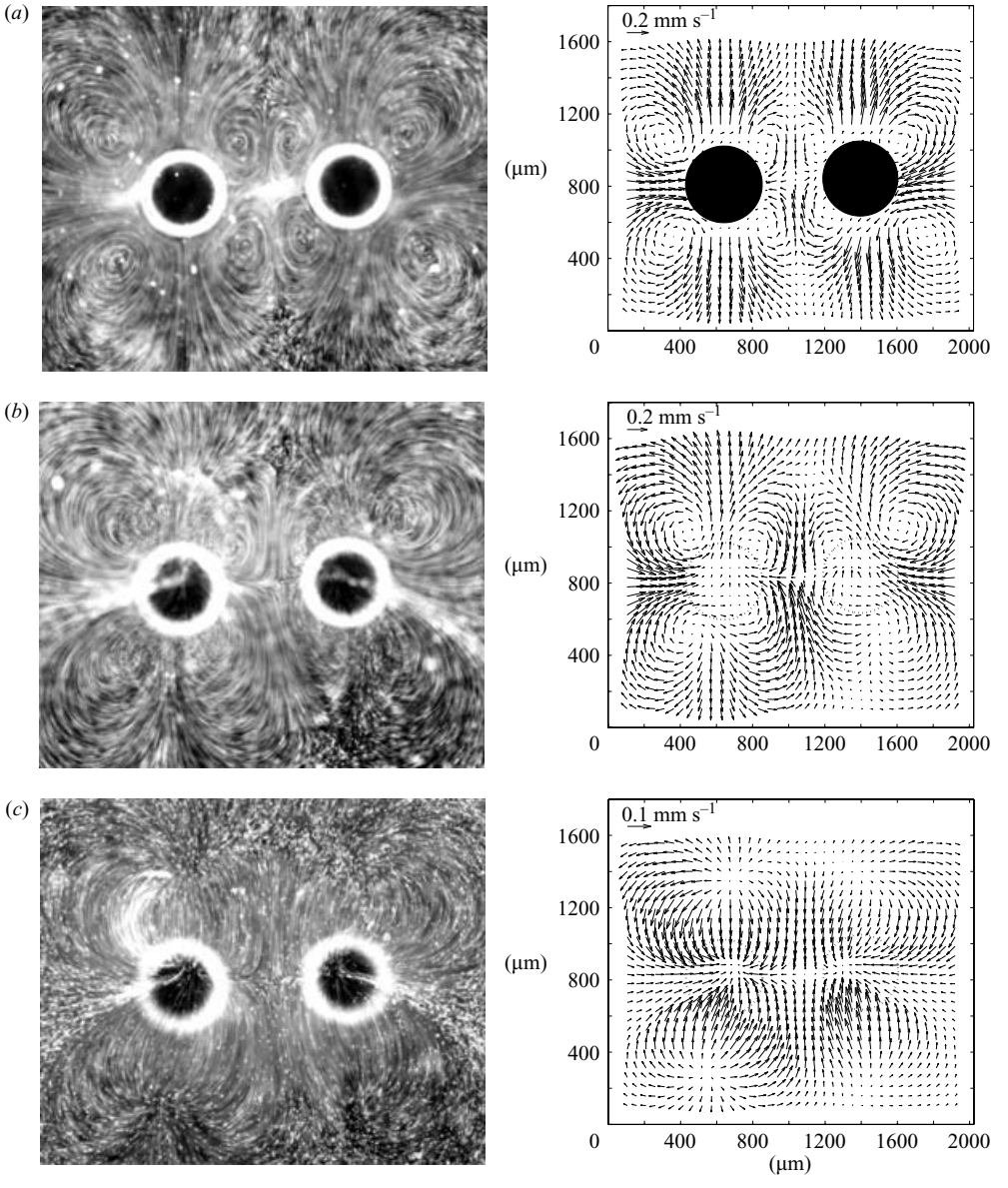

FIGURE 22. Case A: two bubbles undergoing translating oscillations along single axes. Streak photograph and micro-PIV velocity field along the (*a*) z_1-, (*b*) z_2- and (*c*) z_3-planes.

approximately 0.2 mm s^{-1}. Flow along the z_2- and z_3-planes show fluid spiralling in towards the individual bubble centres as they do in the single bubble case.

The centroid positions of the two orbiting bubbles are shown in figure 25 with the orbits moving in an anticlockwise direction. The axis ratios of the orbits are $\lambda = 0.453$ and 0.525 for Bubbles 1 and 2, respectively. These orbits have a major and minor axis of roughly 1.2 % and 0.6 % of the bubble equilibrium radius, respectively. Note that these values of λ are greater than the estimated critical value $\lambda_c = 0.156$–0.186 suggested in § 4.4. It was earlier conjectured that for values of $\lambda > \lambda_c$, the streaming patterns would consist of a streaming pattern consisting of a circulation around the

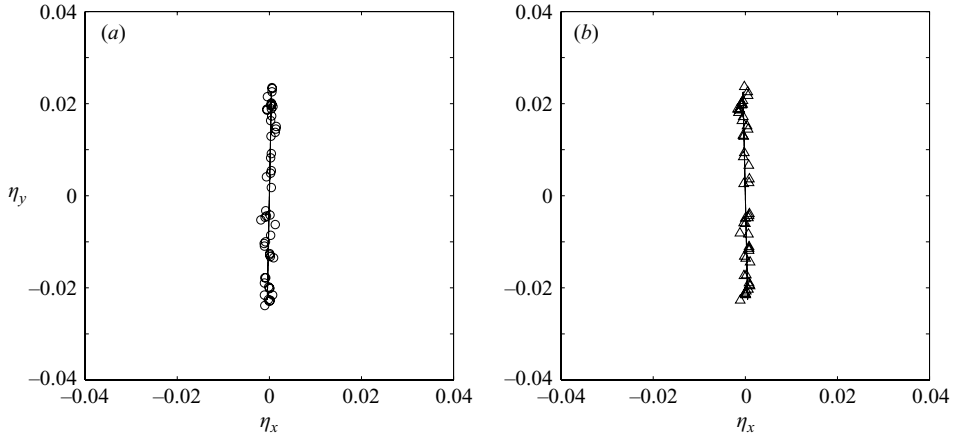

FIGURE 23. Case A: two bubbles undergoing translating oscillations along single axes. Map of the bubble centroid positions η_x and η_y of (a) Bubble 1 and (b) Bubble 2.

Bubble	ϵ_x	ϵ_y	M^2	$R_{s,x}$	$R_{s,y}$	λ
1	0.574×10^{-2}	1.265×10^{-2}	370	1.218×10^{-2}	5.928×10^{-2}	0.453
2	0.612×10^{-2}	1.166×10^{-2}	326	1.498×10^{-2}	5.429×10^{-2}	0.525

TABLE 3. Case B: two bubbles undergoing elliptical orbiting oscillations. Non-dimensional streaming parameters.

bubble, along with two outer vortices. The two outer vortices are not observed in this experiment, and are possibly being suppressed by the presence of the adjacent bubble. A summary of the streaming parameters is shown in table 3 and correspond to $\epsilon \ll 1$, $M^2 \gg 1$ and $R_s \ll 1$. The bubble's radius remains roughly constant throughout the experiment.

5.3. *Case C: two bubbles undergoing volume oscillations*

The final case studied was of two bubbles undergoing a volume oscillation in phase. Bubbles 1 and 2 have an equilibrium radius of 322 μm and 331 μm respectively. The bubbles were excited at an acoustic frequency of 6 kHz and pressure amplitude of 16.96 Pa. The streamlines and velocity fields around the bubbles are shown in figure 26. The streaming flow appears to contain two 'dipole' patterns, as observed for the individual volume oscillating bubble (see § 4.5), directed toward one another which leads to an impingement in the flow between the bubbles.

The direction of the 'dipoles' appears to be dictated by the direction of the small-amplitude translating motion of the bubbles. Figure 27(a) shows that the centroid positions of the bubble have a small movement along the axis connecting the two centres of the bubbles. These fluctuating motions may be attributed to the secondary Bjerknes force (see Doinikov & Zavtrak 1995; Harkin, Kaper & Nadim 2001) which attract or repel the bubbles from one another when they oscillate in phase or antiphase. The variation in the bubble radius over one cycle (figure 27b) shows the bubbles oscillating in phase and at an amplitude of roughly 0.75 % of the bubble equilibrium radius (see table 4).

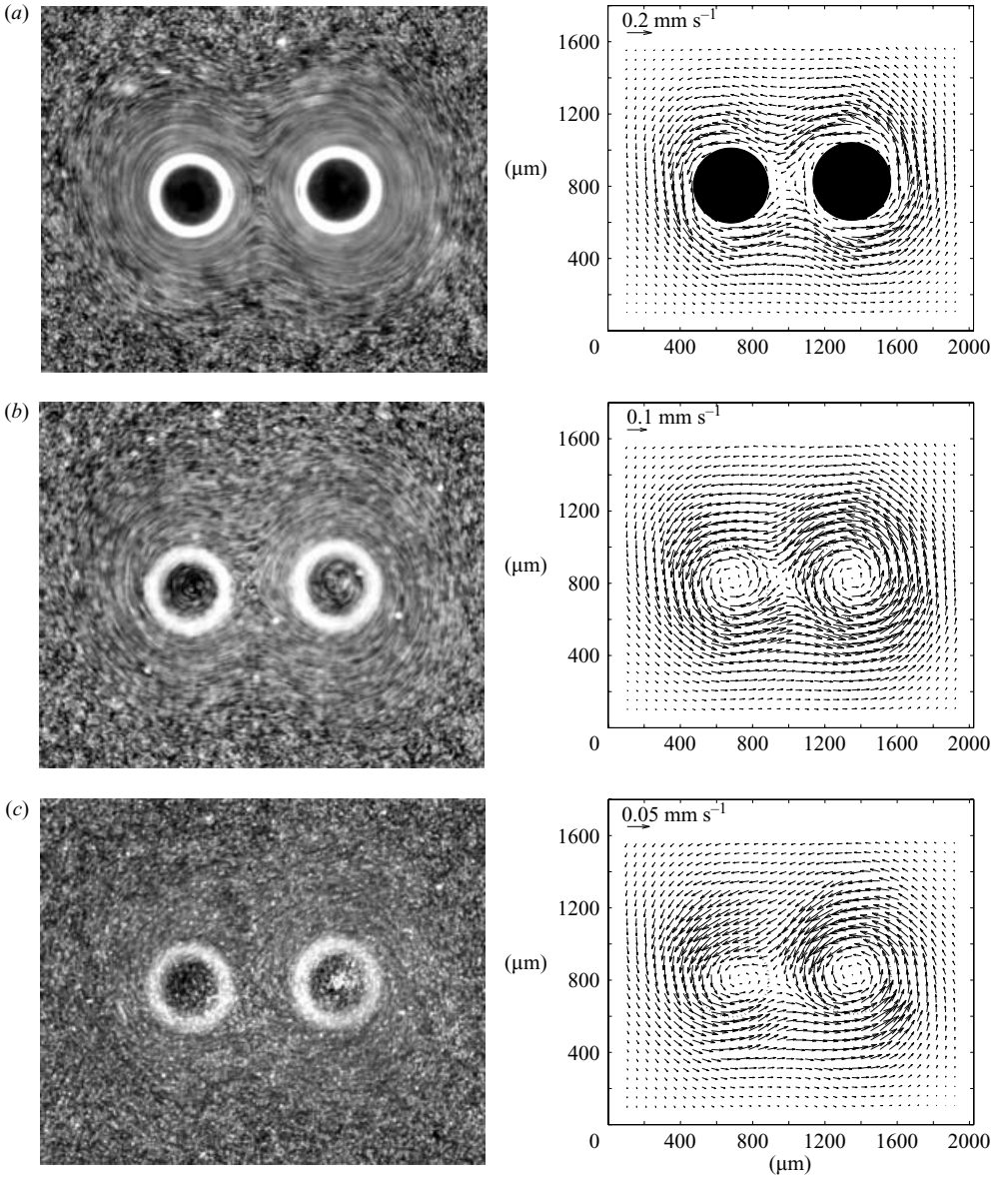

FIGURE 24. Case B: two bubbles undergoing elliptical orbiting oscillations. Streak photograph and micro-PIV velocity field along the (*a*) z_1-, (*b*) z_2- and (*c*) z_3-planes.

Bubble	a_r	b_r	c_r	95 % Confidence limit in a_r
1	0.743×10^{-2}	1.956	-0.765×10^{-3}	$\pm 0.104 \times 10^{-2}$
2	0.773×10^{-2}	2.126	-0.683×10^{-3}	$\pm 0.0973 \times 10^{-2}$

TABLE 4. Case C: two bubbles undergoing volume oscillations. Parameters of the curve fitting of the radius displacements η_r over one cycle.

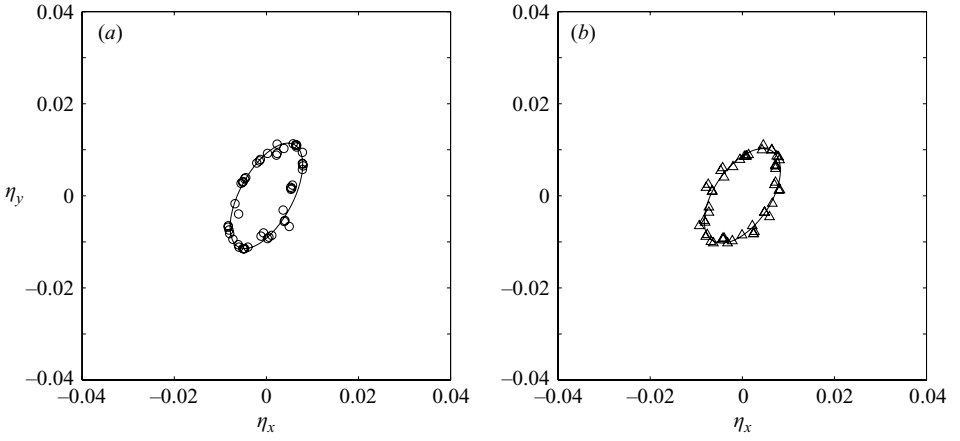

FIGURE 25. Case B: two bubbles undergoing elliptical orbiting oscillations. Map of the centroid positions η_x and η_y of (*a*) Bubble 1 and (*b*) Bubble 2.

Bubble	Initial radius (μm)	f (kHz)	P (Pa)	Initial mode of oscillation
1	200	0	0	Stationary bubble
2	223	2.597	120.25	Translating along a single axis
3	146	13.43	94.30	Radial volume pulsation

TABLE 5. Summary of the different cases of the mass diffusion induced growth of a bubble.

5.4. *Microstreaming around three and four bubbles*

Several experiments were also performed for groups of three and four bubbles in symmetrical arrangements and give similar flow behaviour to the two-bubble cases, i.e. mirroring streaming patterns are also observed. Several of these streaming patterns are shown in figure 28. The streaming flow patterns indicate bubbles that are undergoing linear translating oscillations (figures 28*a* and 28*d*), volume oscillations (figure 28*b*) and orbiting oscillations (figures 28*c* and 28*e*).

6. Growth of an oscillating bubble

During the course of the experiments, it was observed that bubbles would increase in size over a period of time. The rate of growth of the bubble appeared to be enhanced under certain modes of oscillation. In figure 29, the radius of a single bubble was plotted over a period of 1 h using images taken every 30 s. During this period, gas diffuses into the bubble, causing it to grow, but also altering the streaming flow around the bubble. Three different cases are shown. The first case is of a bubble at rest, where the bubble grows purely by static diffusion. Bubbles in free-field conditions tend to dissolve away because the partial pressure of gas in the bubble is above that in the liquid. In this experiment, it is presumably the bubble's attachment to the polycarbonate wall (as a nucleation site) which prevents its dissolution. Therefore, the theories for mass diffusion of a spherical bubble in free-field conditions are inadequate for modelling the bubble growths observed in these experiments. The other two cases are of oscillating bubbles with different streaming flows around them. Table 5 summarizes the different cases studied.

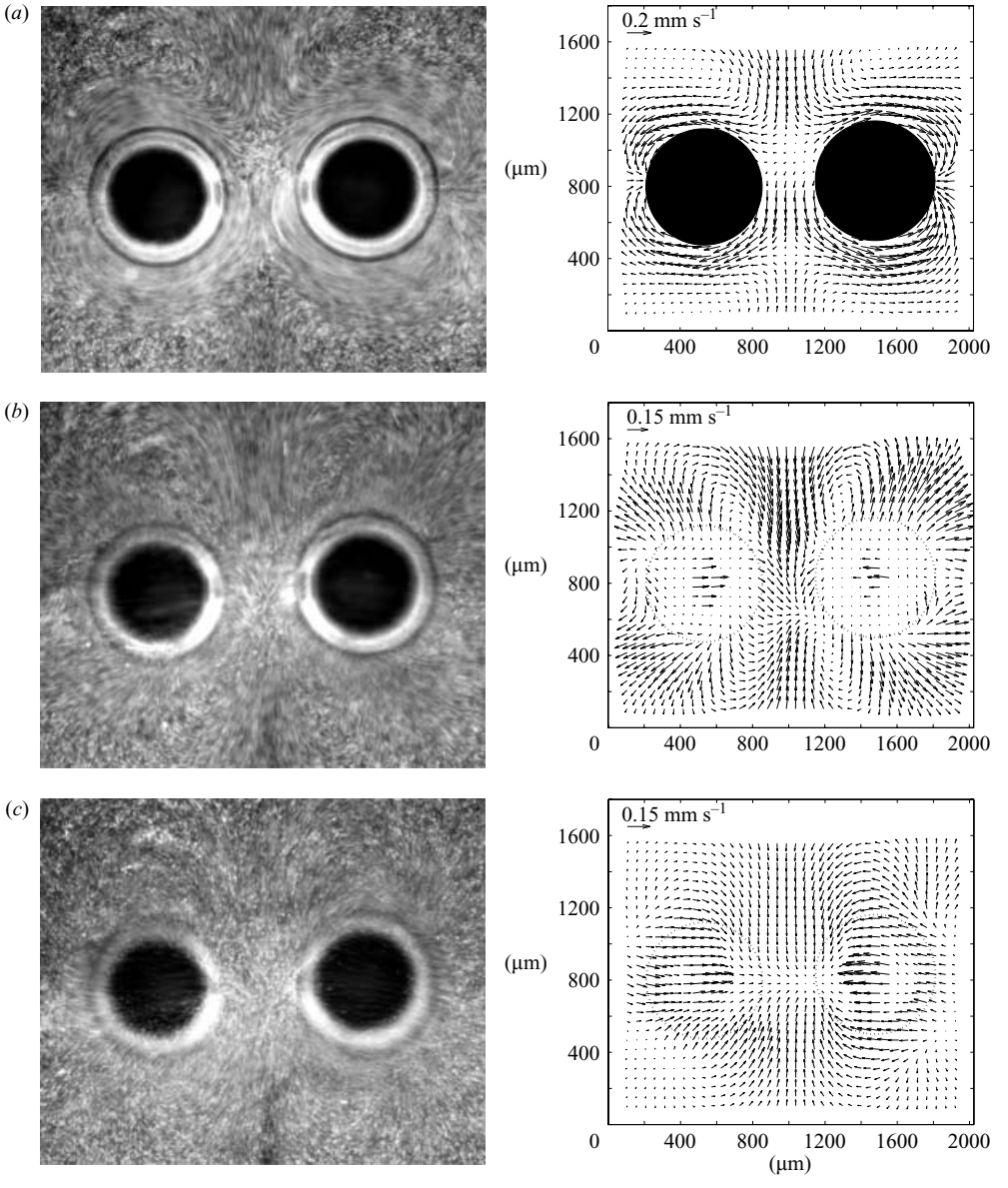

FIGURE 26. Case C: two bubbles undergoing volume oscillations. Streak photograph and micro-PIV velocity field along the (*a*) z_1-, (*b*) z_2- and (*c*) z_3-planes.

There is clearly an enhancement in the growth rate of a bubble owing to the presence of microstreaming flows. The static bubble's radius grows uniformly at a rate of roughly 0.24 μm min^{-1}. The bubble excited at 2.597 kHz shows a steady growth rate of approximately 0.95 μm min^{-1}, roughly four times faster than the growth rate of the static bubble. The streaming flow pattern around this bubble does not vary greatly over the course of the experiment (figure 30). The bubble driven at 13.43 kHz shows the greatest enhancement in growth rate during the first 19 min with a growth rate of approximately 1.71 μm min^{-1} or 7.2 times faster than the static diffusion case. Figure 31(*a*) shows a 'dipole' streaming flow pattern for the first 19 min which is

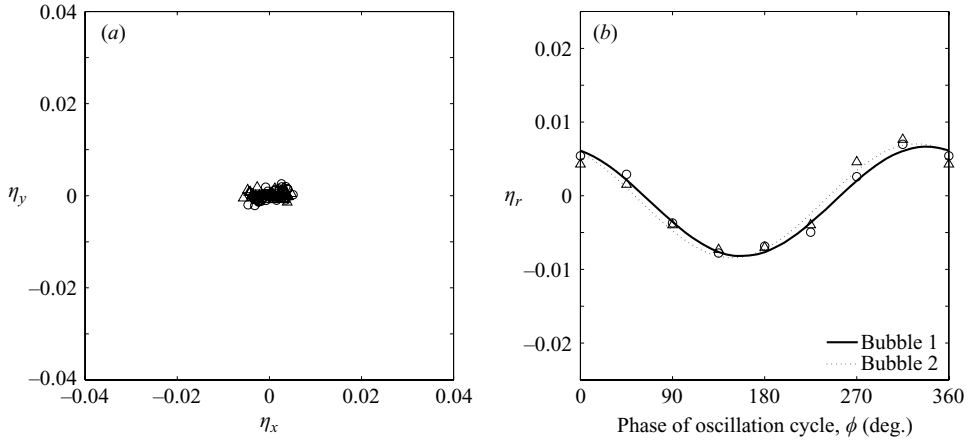

FIGURE 27. Case C: two bubbles undergoing volume oscillations. Plots of the oscillatory motion of the (*a*) centroid and (*b*) radius for Bubble 1 (○) and Bubble 2 (□).

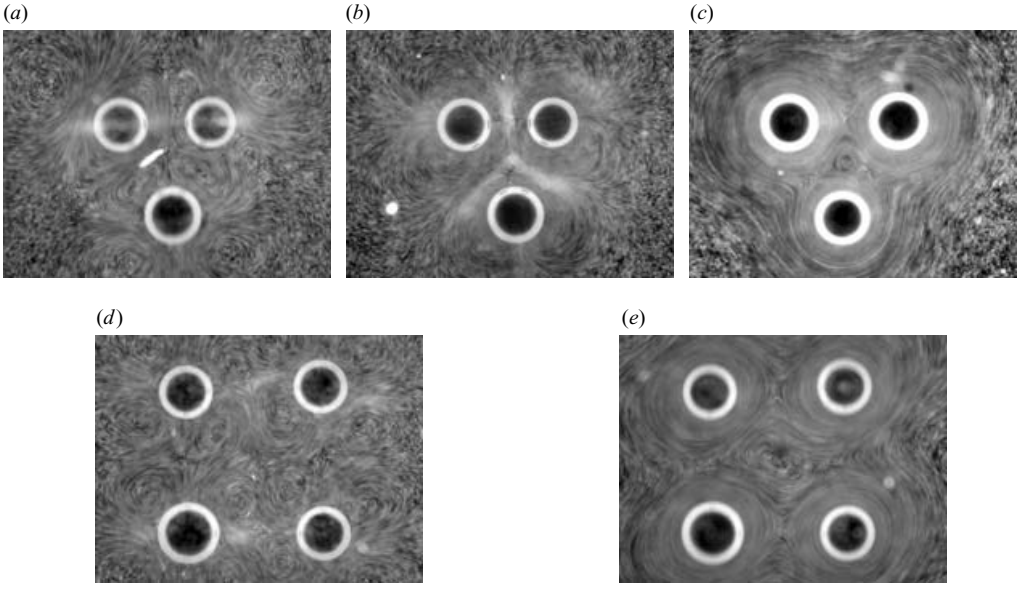

FIGURE 28. Various streaming patterns around three- and four-bubble arrangements.

indicative of a bubble in a volume oscillation mode. After $t = 19$ min, the flow pattern changes to a 'quadrupole' pattern (figure 31*b*), similar to what is observed in a linear translating bubble and there is a corresponding decrease in the growth rate to $0.67\,\mu\mathrm{m\,min^{-1}}$ for the remainder of the test period. The streaming flow pattern around the bubble continues to undergo variations, as shown in figures 31(*c*) and 31(*d*).

The enhancement in growth rates appears to be related to two mechanisms. First, the streaming flows accentuate diffusion by improving the mixing of fluid near the bubble's surface. This ensures that 'fresh' fluid with a high concentration of gas is transported near the air–water interface to maintain the diffusion process. Also the growth rate of the volume oscillating bubble which shows the greatest growth rate

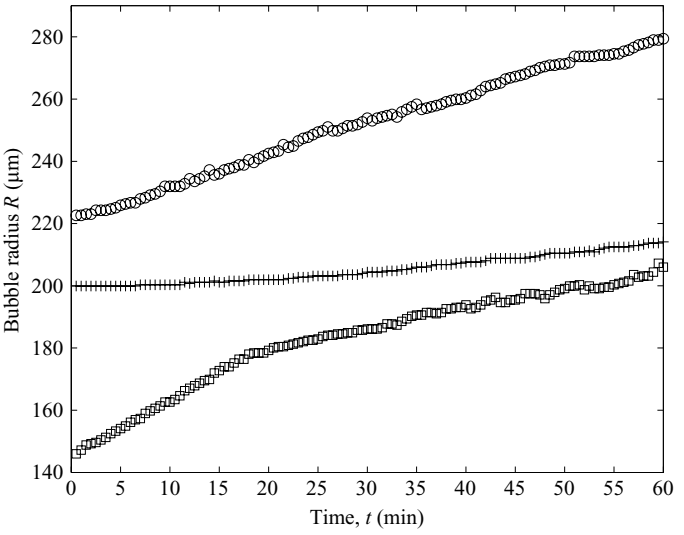

FIGURE 29. Plot of the bubble radius against time. Bubble 1, static bubble (+); Bubble 2, linear translating bubble (○); and Bubble 3, volume oscillating bubble (□).

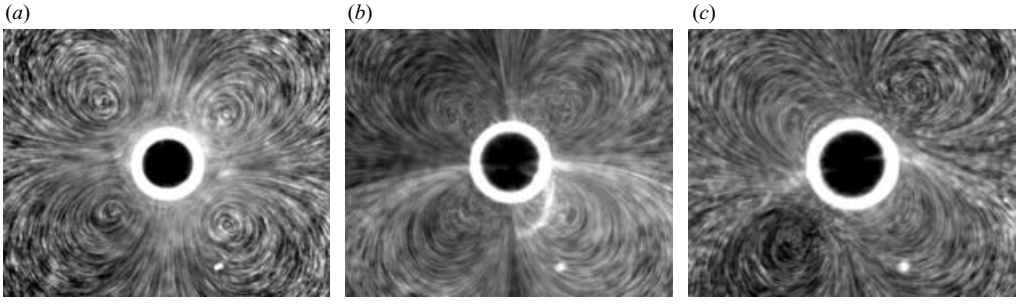

FIGURE 30. Streaming patterns around Bubble 2 excited at 2.597 kHz at times (*a*) $t = 0$ min, (*b*) $t = 30$ min and (*c*) $t = 60$ min.

will also be enhanced by rectified diffusion as well as the microstreaming flows. There is considerable work on the growth of a bubble owing to rectified diffusion (see Eller & Flynn 1965; Eller 1969, 1972, 1975; Crum 1980); however, these studies are of spherical bubbles, rather than bubbles held on solid surfaces which prevent it from dissolution, and do not consider the effects of microstreaming. Gould (1974) experimentally studied the growth rate of a bubble held stationary in a standing wave and which has a microstreaming flow around it. His results show that the growth or dissolution of the bubble depends on the pressure amplitude and the amount of dissolved gas in the liquid. Davidson (1971) studied the effect microstreaming has on mass diffusion for a bubble translating along a single axis and in free-field conditions. His work showed that the effect of microstreaming is to enhance whatever process would occur in the absence of sound (dissolution or growth). The results of these experiments agree with this finding.

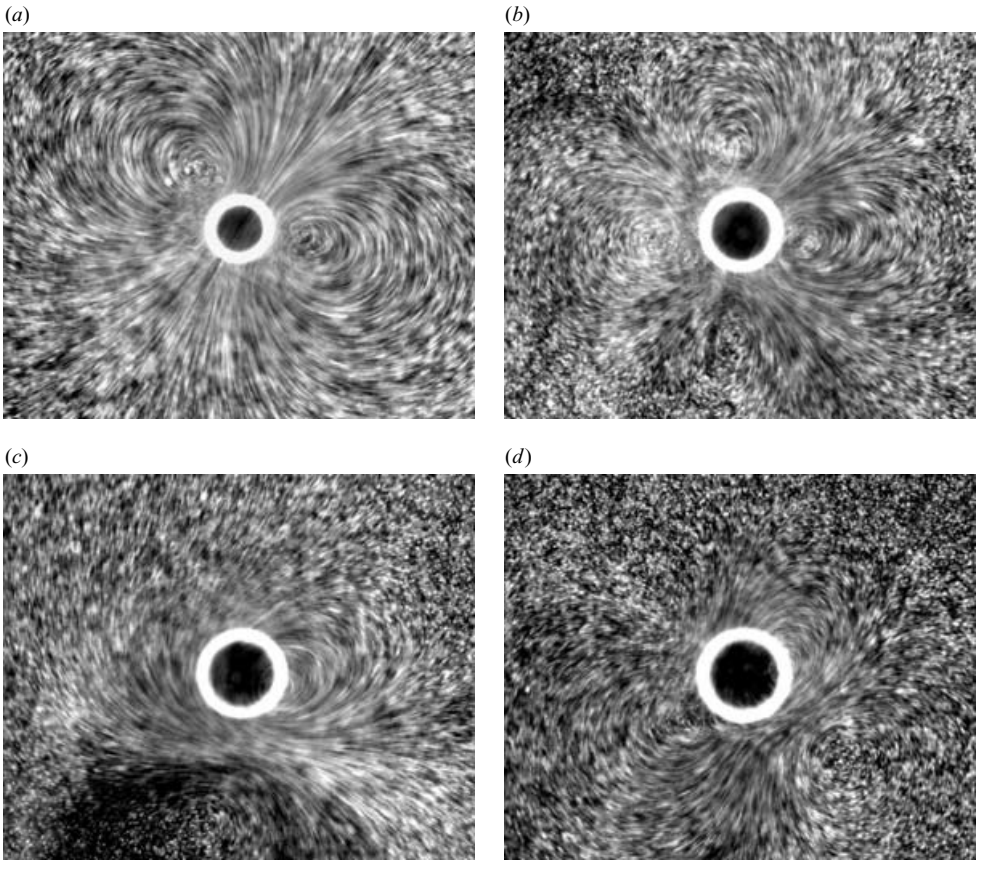

FIGURE 31. Streaming patterns around Bubble 3 excited at 13.43 kHz at times (*a*) $t = 0$ min, (*b*) $t = 19$ min, (*c*) $t = 40$ min and (*d*) $t = 60$ min.

7. Conclusion

Micro-PIV measurements and flow visualization have shown the different microstreaming flow patterns observed around a single bubble and two bubbles resting on a solid boundary. The modes of oscillation that were studied included translating, volume and shape mode oscillations. The streaming flows were observed to be affected by three main parameters: the acoustic excitation frequency, pressure amplitude and the size of the bubble. The streaming patterns mostly vary smoothly as the frequency is varied which gives rise to a wide variety of streaming patterns. Adjustment in the pressure amplitude generally only increases the streaming velocity, while the streaming flow pattern remains unchanged. The only exception to this is when the pressure amplitude exceeds a threshold, in which case, shape mode oscillations are observed.

The translating motions that the centroid of the bubble moves through were described as general elliptical orbits with a minor to major axis ratio λ. It was observed that these elliptical orbits transformed smoothly with the acoustic frequency from say a translation along a single axis, to an elliptical orbit and finally to a circular orbit, corresponding to a gradual increase from $\lambda = 0$ to 1. As the value of λ increases from a linear translation, the streaming flow pattern gradually changes from a 'quadrupole' pattern, to a skewed 'quadrupole' pattern, then to an elliptical vortex

and finally to a circular vortex around the bubble. There appears to be a critical value in λ as the ellipse shape is varied between the skewed 'quadrupole' streaming pattern and the elliptical vortex surrounding the bubble. The experiments suggest a value of $\lambda_c = 0.156$–0.186. The results of the experiments appear to have some inconsistencies with established theoretical studies. It appears that the bubbles in the experiments may have different boundary conditions to that of a 'clean' bubble as the streaming flow in the linear translating bubble moves in the opposite direction to what is predicted for a bubble, but matches the streaming flow direction for a solid sphere.

Volume modes of oscillation were also studied with the radius of the bubble oscillating sinusoidally with the same frequency as the acoustic frequency and with an amplitude of the order of 1 % of the bubble's equilibrium radius. The streaming patterns appear to be 'dipole' structures and share similar features to those predicted by Wu & Du (1997) and Longuet-Higgins (1998). Several shape mode oscillations were also briefly studied. These appear to be the $n = 6$, 7 and 8 modes. The streaming flows observed were several times faster than what was observed in the translating and volume modes of oscillation. These studies also covered the flow around two-, three- and four-bubble arrangements and include bubbles undergoing translations along single axes, elliptical orbits and volume oscillations.

The authors wish to acknowledge the assistance of Dr Yonggang Zhu, who set up the micro-PIV system at the CSIRO Microfluidics Laboratory and conducted some closely related experiments.

REFERENCES

Adrian, R. J. 1991 Particle-imaging techniques for experimental fluid mechanics. *Annu. Rev. Fluid Mech.* **23**, 261–304.

Adrian, R. J. & Yao, C. D. 1985 Pulsed laser technique application to liquid and gasesous flows and the scattering power of seed materials. *Appl. Opt.* **24**, 44–52.

Amin, N. 1988 Low frequency oscillations of a cylinder in a viscous fluid. *Q. J. Mech. Appl. Maths* **41**, 195–201.

Birkin, P. R., Watson, Y. E., Leighton, T. G. & Smith, K. L. 2002 Electrochemical detection of Faraday waves on the surface of a gas bubble. *Langmuir* **18**, 2135–2140.

Canny, J. 1986 A computational approach to edge detection. *IEEE Trans. Pattern Anal. Machine Intell.* **8**, 679–698.

Crum, L. A. 1980 Measurements of the growth of air bubbles by rectified diffusion. *J. Acoust. Soc. Am.* **68**, 203–211.

Davidson, B. J. 1971 Mass transfer due to cavitation microstreaming. *J. Sound Vib.* **17**, 261–270.

Davidson, B. J. & Riley, N. 1971 Cavitation microstreaming. *J. Sound Vib.* **15**, 217–233.

Davidson, B. J. & Riley, N. 1972 Jets induced by oscillatory motions. *J. Fluid Mech.* **53**, 287–303.

Devasenathipathy, S., Santiago, J. G., Wereley, S. T., Meinhart, C. D. & Takehara, K. 2003 Particle imaging techniques for microfabricated fluidic systems. *Exps. Fluids* **34**, 504–514.

Doinikov, A. 2004 Translational motion of a bubble undergoing shape oscillations. *J. Acoust. Soc. Am.* **501**, 1–24.

Doinikov, A. & Zavtrak, S. T. 1995 On the mutual interaction of two gas bubbles in sound field. *Phys. Fluids* **7**, 1923–1930.

Elder, S. A. 1959 Cavitation microstreaming. *J. Acoust. Soc. Am.* **31**, 54–64.

Eller, A. I. 1969 Growth of bubbles by rectified diffusion. *J. Acoust. Soc. Am.* **46**, 1246–1250.

Eller, A. I. 1972 Bubble growth by diffusion in an 11-kHz sound field. *J. Acoust. Soc. Am.* **52**, 1447–1449.

Eller, A. I. 1975 Effects of diffusion on gaseous cavitation bubbles. *J. Acoust. Soc. Am.* **57**, 1374–1378.

Eller, A. I. & Crum, L. A. 1970 Instability of the motion of a pulsating bubble in a sound field. *J. Acoust. Soc. Am.* **47**, 762–767.

Eller, A. I. & Flynn, H. G. 1965 Rectified diffusion during nonlinear pulsations of cavitation bubbles. *J. Acoust. Soc. Am.* **37**, 493–503.

Francescutto, A. & Nabergoj, R. 1978 Pulsation amplitude threshold for surface waves on oscillating bubbles. *Acustica* **41**, 215–220.

Gormley, G. & Wu, J. 1998 Acoustic streaming near Albunex spheres. *J. Acoust. Soc. Am.* **104**, 3115–3118.

Gould, R. K. 1974 Rectified diffusion in the presence of, and absence of, acoustic streaming. *J. Acoust. Soc. Am.* **56**, 1740–1746.

Harkin, A., Kaper, T. J. & Nadim, A. 2001 Coupled pulsation and translation of two gas bubbles in liquid. *J. Fluid Mech.* **445**, 377–411.

Holtsmark, J., Johnsen, I., Sikkeland, T. & Skavlem, S. 1954 Boundary layer flow near a cylindrical obstacle in an oscillating incompressible fluid. *J. Acoust. Soc. Am.* **26**, 26–39.

Kolb, J. & Nyborg, W. 1956 Small-scale acoustic streaming in liquids. *J. Acoust. Soc. Am.* **28**, 1237–1242.

Kornfeld, M. & Suvorov, L. 1944 On the destructive action of cavitation. *J. Acoust. Soc. Am.* **15**, 495–506.

Lee, C. P. & Wang, T. G. 1989 Near-boundary streaming around a small sphere due to two orthogonal standing waves. *J. Acoust. Soc. Am.* **85**, 1081–1088.

Lee, C. P. & Wang, T. G. 1990 Outer acoustic streaming. *J. Acoust. Soc. Am.* **88**, 2367–2375.

Lewin, P. A. & Bjørnø, L. 1982 Acoustically induced shear stresses in the vicinity of microbubbles in tissue. *J. Acoust. Soc. Am.* **71**, 728–734.

Liu, R. H., Yang, J., Pindera, M. Z., Athavale, M. & Grodzinski, P. 2002 Bubble-induced acoustic micromixing. *Lab Chip* **2**, 151–157.

Longuet-Higgins, M. S. 1998 Viscous streaming from an oscillating spherical bubble. *Proc. R. Soc. Lond.* A **454**, 725–742.

Marmottant, P. & Hilgenfeldt, S. 2003 Controlled vesicle deformation and lysis by single oscillating bubbles. *Nature (Lond.)* **423**, 153–156.

Marmottant, P. & Hilgenfeldt, S. 2004 A bubble-driven microfluidic transport element for bioengineering. *Proc. Natl. Acad. Sci.* **101**, 9523–9527.

Marston, P. L. 1980 Shape oscillation and static deformation of drops and bubbles driven by modulated radiation stresses – theory. *J. Acoust. Soc. Am.* **67**, 15–26.

Meinhart, C. D., Wereley, S. T. & Gray, M. H. B. 2000 Volume illumination for two-diemnsional particle image velocimetry. *Meas. Sci. Technol.* **11**, 809–814.

Minnaert, M. 1933 On musical air bubbles and the sound of running water. *Phil. Mag.* **16**, 235–248.

Nyborg, W. 1965 Acoustic streaming. In *Physical Acoustics IIB* (ed. W. P. Mason), pp. 265–331. Academic.

Nyborg, W. 1998 Acoustic streaming. In *Nonlinear Acoustics* (ed. M. F. Hamilton & D. T. Blackstock), pp. 207–231. Academic.

Pritchard, N. J., Hughes, D. E. & Peacocke, A. R. 1966 The ultrasonic degradation of biological macromolecules under conditions of stable cavitation. i. Theory, methods, and application to deoxyribonucleic acid. *Biopolymers* **4**, 259–274.

Riley, N. 1965 Oscillating viscous flows. *Mathematika* **12**, 161–175.

Riley, N. 1966 On a sphere oscillating in a viscous fluid. *Q. J. Mech. Appl. Maths.* **19**, 461–472.

Riley, N. 1967 Oscillatory viscous flows. review and extension. *J. Inst. Math. Applics.* **3**, 419–434.

Riley, N. 1971 Stirring of a viscous fluid. *Z. Angew. Math. Phys.* **22**, 645–653.

Riley, N. 1975 The steady streaming induced by a vibrating cylinder. *J. Fluid Mech.* **68**, 801–812.

Riley, N. 1992 Acoustic streaming about a cylinder in orthogonal beams. *J. Fluid Mech.* **242**, 387–394.

Riley, N. 2001 Steady streaming. *Annu. Rev. Fluid Mech.* **33**, 43–65.

Rooney, J. A. 1989 Shear as a mechanism for sonically induced biological effects. *J. Acoust. Soc. Am.* **52**, 1718–1724.

Rosenthal, I., Sostaric, J. Z. & Riesz, P. 2004 Enlightened sonochemistry. *Res. Chem. Intermed.* **30**, 685–701.

Shoh, A. 1975 Industrial applications of ultrasound – a review. *IEEE Trans. Sonics Ultrasonics* **22**, 60–71.

Strasberg, M. & Benjamin, T. B. 1958 Excitation of oscillations in the shape of pulsating gas bubbles. *J. Acoust. Soc. Am.* **30**, 697.

Thiessen, D. B. & Man, K. F. 1998 Surface tension measurement. In *The Measurement, Instrumentation, and Sensors Handbook* (ed. J. G. Webster). CRC.

Tho, P. 2005 Cavitation microstreaming in single and two bubble systems. Master's thesis, The University of Melbourne.

Verraes, T., Lepoint-Mullie, F., Lepoint, T. & Longuet-Higgins, M. S. 2000 Experimental study of the liquid flow near a single sonoluminescent bubble. *J. Acoust. Soc. Am.* **108**, 118–125.

Watson, Y. E., Birkin, P. R. & Leighton, T. G. 2003 Electrochemical detection of bubble oscillation. *Ultrasonics Sonochem.* **10**, 65–69.

Wereley, S. T. & Meinhart, C. D. 2003 Micron-resolution particle image velocimetry. In *Micro- and Nano-Scale Diagnostic Techniques* (ed. K. S. Breuer). Springer.

Wu, J. 2002 Theoretical study on shear stress generated by microstreaming surrounding contrast agents attached to living cells. *Ultrasound Med. Bio.* **28**, 125–129.

Wu, J. & Du, G. 1997 Streaming generated by a bubble in an ultrasound field. *J. Acoust. Soc. Am.* **101**, 1899–1907.

Wu, J., Ross, J. P. & Chiu, J. F. 2002 Reparable sonoporation generated by microstreaming. *J. Acoust. Soc. Am.* **111**, 1460–1464.